



## Article

# Development of $\text{La}_{1.7}\text{Ca}_{0.3}\text{Ni}_{1-y}\text{Cu}_y\text{O}_{4+\delta}$ Materials for Oxygen Permeation Membranes and Cathodes for Intermediate-Temperature Solid Oxide Fuel Cells

Elena Filonova <sup>1</sup>, Artem Gilev <sup>2</sup>, Tatyana Maksimchuk <sup>3,4</sup>, Nadezhda Pikalova <sup>5</sup>, Kiryl Zakharchuk <sup>6</sup>, Sergey Pikalov <sup>5</sup>, Aleksey Yaremchenko <sup>6</sup> and Elena Pikalova <sup>3,7,\*</sup>

- <sup>1</sup> Department of Physical and Inorganic Chemistry, Institute of Natural Sciences and Mathematics, Ural Federal University, 620002 Yekaterinburg, Russia
  - <sup>2</sup> Laboratory of Chemical Design of New Multifunctional Materials, Institute of Natural Sciences and Mathematics, Ural Federal University, 620002 Yekaterinburg, Russia
  - <sup>3</sup> Institute of High Temperature Electrochemistry, Ural Branch of the Russian Academy of Sciences, 620137 Yekaterinburg, Russia
  - <sup>4</sup> Department of Chemical Materials Science, Institute of Natural Sciences and Mathematics, Ural Federal University, 620002 Yekaterinburg, Russia
  - <sup>5</sup> Institute of Metallurgy, Ural Branch of the Russian Academy of Sciences, 620016 Yekaterinburg, Russia
  - <sup>6</sup> CICECO—Aveiro Institute of Materials, Department of Materials and Ceramic Engineering, University of Aveiro, 3810-193 Aveiro, Portugal
  - <sup>7</sup> Department of Environmental Economics, Graduate School of Economics and Management, Ural Federal University, 620002 Yekaterinburg, Russia
- \* Correspondence: e.pikalova@list.ru



**Citation:** Filonova, E.; Gilev, A.; Maksimchuk, T.; Pikalova, N.; Zakharchuk, K.; Pikalov, S.; Yaremchenko, A.; Pikalova, E. Development of  $\text{La}_{1.7}\text{Ca}_{0.3}\text{Ni}_{1-y}\text{Cu}_y\text{O}_{4+\delta}$  Materials for Oxygen Permeation Membranes and Cathodes for Intermediate-Temperature Solid Oxide Fuel Cells. *Membranes* **2022**, *12*, 1222. <https://doi.org/10.3390/membranes12121222>

Academic Editor: Ahmad Fauzi Ismail

Received: 14 October 2022  
Accepted: 28 November 2022  
Published: 2 December 2022

**Publisher's Note:** MDPI stays neutral with regard to jurisdictional claims in published maps and institutional affiliations.



**Copyright:** © 2022 by the authors. Licensee MDPI, Basel, Switzerland. This article is an open access article distributed under the terms and conditions of the Creative Commons Attribution (CC BY) license (<https://creativecommons.org/licenses/by/4.0/>).

**Abstract:** The  $\text{La}_{1.7}\text{Ca}_{0.3}\text{Ni}_{1-y}\text{Cu}_y\text{O}_{4+\delta}$  ( $y = 0.0\text{--}0.4$ ) nickelates, synthesized via a solid-state reaction method, are investigated as prospective materials for oxygen permeation membranes and IT-SOFC cathodes. The obtained oxides are single-phase and possess a tetragonal structure ( $I4/mmm$  sp. gr.). The unit cell parameter  $c$  and the cell volume increase with Cu-substitution. The interstitial oxygen content and total conductivity decrease with Cu-substitution. The low concentration of mobile interstitial oxygen ions results in a limited oxygen permeability of Cu-substituted  $\text{La}_{1.7}\text{Ca}_{0.3}\text{NiO}_{4+\delta}$  ceramic membranes. However, increasing the Cu content over  $y = 0.2$  induces two beneficial effects: enhancement of the electrochemical activity of the  $\text{La}_{1.7}\text{Ca}_{0.3}\text{Ni}_{1-y}\text{Cu}_y\text{O}_{4+\delta}$  ( $y = 0.0; 0.2; 0.4$ ) electrodes and decreasing the sintering temperature from  $1200\text{ }^\circ\text{C}$  to  $900\text{ }^\circ\text{C}$ . Enhanced electrode activity is due to better sintering properties of the developed materials ensuring excellent adhesion and facilitating the charge transfer at the electrode/electrolyte interface and, probably, faster oxygen exchange in Cu-rich materials. The polarization resistance of the  $\text{La}_{1.7}\text{Ca}_{0.3}\text{Ni}_{1.6}\text{Cu}_{0.4}\text{O}_{4+\delta}$  electrode on the  $\text{Ce}_{0.8}\text{Sm}_{0.2}\text{O}_{1.9}$  electrolyte is as low as  $0.15\text{ }\Omega\text{ cm}^2$  and  $1.95\text{ }\Omega\text{ cm}^2$  at  $850\text{ }^\circ\text{C}$  and  $700\text{ }^\circ\text{C}$  in air, respectively. The results of the present work demonstrate that the developed  $\text{La}_{1.7}\text{Ca}_{0.3}\text{Ni}_{0.6}\text{Cu}_{0.4}\text{O}_{4+\delta}$ -based electrode can be considered as a potential cathode for intermediate-temperature solid oxide fuel cells.

**Keywords:** SOFCs; solid oxide fuel cells; cathodes; lanthanum nickelate; oxygen permeation membrane; electroconductivity; oxygen permeability; polarization resistance; electrode microstructure; collector layer

## 1. Introduction

The growing demand for highly efficient, clean, and renewable energy sources requires increasingly intensive development of sustainable routes, including hydrogen [1,2], and alternative energy generation based on natural [3–5] and biofuels [6,7]. Hydrogen energy has an advantage among the listed technologies of the future since  $\text{H}_2$  is one of the common and abundant elements in nature and is a universal energy carrier [1,8].

Among various hydrogen-based energy production and conversion systems, solid oxide fuel cells (SOFCs) are recognized as one of the most promising technologies due to the

numerous environmental and technical advantages they offer [9–11]. The main superiorities of SOFCs include high efficiency [12,13] and the ability to be used, along with hydrogen, with a wide variety of fuels such as hydrocarbons, natural gas, biogas, etc. [14–16].

However, the industrial commercialization of SOFCs is limited due to their performance reduction with time at high operating temperatures (800–1000 °C). This is a result of the degradation of SOFC structural parts [17,18], the main contribution to which is made by the chemical interaction between them [19]. Reducing the operating temperatures of SOFCs to 600–800 °C by selecting new functional materials would improve the durability of SOFCs and reduce their costs [14,20]. However, lowering the operating temperature leads to an increase in the activation energy of the oxygen reduction reaction (ORR) and an increase in the area-specific resistance of the electrodes (ASR), especially of the cathode. The use of oxide materials with mixed electron-ionic conductivity (MIEC) as cathodes can significantly improve surface oxygen exchange kinetics due to the expanded zone of electrochemical reactions, thus enabling the efficient operation of SOFCs at intermediate and low temperatures [21].

Due to the ambipolar conductivity, complex oxides with the Ruddlesden–Popper structure  $\text{Ln}_2\text{NiO}_{4+\delta}$  (Ln = La, Pr, Nd) and their substituted derivatives have been successfully tested as cathode materials either for intermediate-temperature fuel cells (IT-SOFCs) with oxygen-ion [22,23] and proton-conducting [24–26] electrolytes, or solid oxide electrolysis cells (SOEC) [24,27], as well as oxygen permeation membranes [28].

Among  $\text{Ln}_2\text{NiO}_{4+\delta}$  (Ln = La, Pr, Nd), it is the phase with Ln = La, which demonstrates the highest thermal stability (up to 1300 °C both in air and in atmospheres with a reduced oxygen content [29]). The literature data, summarized in Table 1, show that the substitutions into the La sublattice with divalent foreign cations such as alkaline earth ones (M =  $\text{Ca}^{2+}$ ,  $\text{Sr}^{2+}$ ,  $\text{Ba}^{2+}$ ) result in an increase in the total electrical conductivity of the  $\text{La}_{2-x}\text{M}_x\text{NiO}_{4+\delta}$  oxides, which is an important functional property for both oxygen permeation membranes and air electrodes.

**Table 1.** Total conductivity and electrode polarization resistance of  $\text{La}_{2-x}\text{M}_x\text{NiO}_{4+\delta}$  (M = Ca, Sr, Ba) nickelates at 700 °C.

M	x	Composition	Ref.	$\sigma, \text{S cm}^{-1}$	$R_p, \Omega \text{ cm}^2$	Electrolyte/Collector
-	0.0	$\text{La}_2\text{NiO}_{4+\delta}$	[30]	65		
-	0.0	$\text{La}_2\text{NiO}_{4+\delta}$	[31]	56	0.73	$\text{Ce}_{0.8}\text{Sm}_{0.2}\text{O}_{1.9}/\text{LNF}$
-	0.0	$\text{La}_2\text{NiO}_{4+\delta}$	[32]	76	0.10	$\text{BaCe}_{0.5}\text{Zr}_{0.3}\text{Dy}_{0.2}\text{O}_{3-\delta}$
-	0.0	$\text{La}_2\text{NiO}_{4+\delta}$	[33]	53	5.75	LSGM
Ca	0.1	$\text{La}_{1.9}\text{Ca}_{0.1}\text{NiO}_{4+\delta}$	[34]	67	1.78	$\text{Ce}_{0.8}\text{Sm}_{0.2}\text{O}_{1.9}/\text{LNF}$
Ca	0.3	$\text{La}_{1.7}\text{Ca}_{0.3}\text{NiO}_{4+\delta}$	[35]	86	12.4	$\text{Ce}_{0.8}\text{Sm}_{0.2}\text{O}_{1.9}$
Ca	0.3	$\text{La}_{1.7}\text{Ca}_{0.3}\text{NiO}_{4+\delta}$	[36]	86	4.01	$\text{Ce}_{0.8}\text{Sm}_{0.2}\text{O}_{1.9}/\text{LNF}$
Ca	0.3	$\text{La}_{1.7}\text{Ca}_{0.3}\text{NiO}_{4+\delta}$	[37]		1.4	LSGM
Ca	0.5	$\text{La}_{1.5}\text{Ca}_{0.5}\text{NiO}_{4+\delta}$	[38]	150	0.061	$\text{BaZr}_{0.1}\text{Ce}_{0.7}\text{Y}_{0.2}\text{O}_{3-\delta}$
Sr	0.3	$\text{La}_{1.7}\text{Sr}_{0.3}\text{NiO}_{4+\delta}$	[35]	69	12.8	$\text{Ce}_{0.8}\text{Sm}_{0.2}\text{O}_{1.9}$
Sr	0.5	$\text{La}_{1.5}\text{Sr}_{0.5}\text{NiO}_{4+\delta}$	[38]	140	0.128	$\text{BaZr}_{0.1}\text{Ce}_{0.7}\text{Y}_{0.2}\text{O}_{3-\delta}$
Sr	0.75	$\text{La}_{1.25}\text{Sr}_{0.75}\text{NiO}_{4+\delta}$	[30]	253		
Sr	1.6	$\text{La}_{0.4}\text{Sr}_{1.6}\text{NiO}_{4+\delta}$	[39]	224	7.9	$\text{Ce}_{0.9}\text{Gd}_{0.1}\text{O}_{2-\delta}$
Ba	0.05	$\text{La}_{1.95}\text{Ba}_{0.05}\text{NiO}_{4+\delta}$	[40]	73	1.11	$\text{BaCe}_{0.5}\text{Zr}_{0.3}\text{Dy}_{0.2}\text{O}_{3-\delta}$
Ba	0.3	$\text{La}_{1.7}\text{Ba}_{0.3}\text{NiO}_{4+\delta}$	[35]	70	16.1	$\text{Ce}_{0.8}\text{Sm}_{0.2}\text{O}_{1.9}$
Ba	0.5	$\text{La}_{1.5}\text{Ba}_{0.5}\text{NiO}_{4+\delta}$	[38]	124	0.127	$\text{BaZr}_{0.1}\text{Ce}_{0.7}\text{Y}_{0.2}\text{O}_{3-\delta}$

Although the polarization resistance of the corresponding  $\text{La}_{2-x}\text{M}_x\text{NiO}_{4+\delta}$  electrodes often increases, it was shown by the methods of thermogravimetry and temperature-programmed isotope exchange [31,36,41,42], that the drop in the electrochemical activity of the  $\text{La}_{2-x}\text{M}_x\text{NiO}_{4+\delta}$  electrodes with the increasing content of dopant was due to a decrease in the content of highly mobile interstitial oxygen.

The data in Table 1 show that among the lanthanum nickelates, substituted with alkaline earth cations, the highest electrochemical activity (the lowest polarization resistance,

$R_p$ ) of the corresponding electrodes in contact with a conventional oxygen-ion conducting  $\text{Ce}_{0.8}\text{Sm}_{0.2}\text{O}_{1.9}$  (SDC) electrolyte for IT-SOFCs is observed for the  $\text{La}_{2-x}\text{Ca}_x\text{NiO}_{4+\delta}$  oxides. This fact stimulated a number of works aimed at the study of the electrical properties and electrochemical activity of the electrodes based on the Ca-doped  $\text{La}_2\text{NiO}_{4+\delta}$  derivatives obtained by the partial substitution of nickel by copper (Table 2). Simultaneous substitution by calcium into the La sublattice and by copper into the Ni sublattice was shown to have advantages in increasing the total conductivity of ceramics and improving the electrochemical activity of the corresponding electrodes in contact with the IT-SOFC electrolytes.

The data presented in Table 1 demonstrate that the  $\text{La}_{2-x}\text{Ca}_x\text{NiO}_{4+\delta}$  electrodes with an oxide collector layer of  $\text{LaNi}_{0.6}\text{Fe}_{0.4}\text{O}_{3-\delta}$  (LNF) exhibited better electrochemical activity than one-layer electrodes, as its use provided uniform current collection in the studied bi-layer electrodes [34–36]. On the other hand, analysis of the characteristics of the previously studied Cu-doped  $\text{La}_{2-x}\text{Ca}_x\text{NiO}_{4+\delta}$  electrodes in contact with a number of electrolytes for IT-SOFCs shown in Table 2 indicated that the  $\text{La}_{1.7}\text{Ca}_{0.3}\text{Ni}_{1-y}\text{Cu}_y\text{O}_{4+\delta}$  electrodes in contact with the  $\text{Ce}_{0.8}\text{Gd}_{0.2}\text{O}_{1.9}$  solid electrolyte successfully operated without a collector layer [43].

**Table 2.** Total conductivity and electrode polarization resistance of  $\text{La}_{2-x}\text{Ca}_x\text{NiO}_{4+\delta}$  nickelates at 700 °C on Cu content (y).

x	y	Composition	Ref.	$\sigma$ , S $\text{cm}^{-1}$	$R_p$ , $\Omega \text{ cm}^2$	Electrolyte
0.0	0.1	$\text{La}_2\text{Ni}_{0.9}\text{Cu}_{0.1}\text{O}_{4+\delta}$	[32]	58	0.16	$\text{BaCe}_{0.5}\text{Zr}_{0.3}\text{Dy}_{0.2}\text{O}_{3-\delta}$
0.0	0.2	$\text{La}_2\text{Ni}_{0.8}\text{Cu}_{0.2}\text{O}_{4+\delta}$	[32]	61	0.5	$\text{BaCe}_{0.5}\text{Zr}_{0.3}\text{Dy}_{0.2}\text{O}_{3-\delta}$
0.0	0.2	$\text{La}_2\text{Ni}_{0.8}\text{Cu}_{0.2}\text{O}_{4+\delta}$	[33]	28	4.95	LSGM
0.0	0.2	$\text{La}_2\text{Ni}_{0.8}\text{Cu}_{0.2}\text{O}_{4+\delta}$	[44]	73	2.0	LSGM
0.0	0.2	$\text{La}_2\text{Ni}_{0.8}\text{Cu}_{0.2}\text{O}_{4+\delta}$	[44]	73	3.2	$\text{La}_{10}\text{Si}_5\text{AlO}_{26.5}$
0.0	0.3	$\text{La}_2\text{Ni}_{0.7}\text{Cu}_{0.3}\text{O}_{4+\delta}$	[32]	55	1.2	$\text{BaCe}_{0.5}\text{Zr}_{0.3}\text{Dy}_{0.2}\text{O}_{3-\delta}$
0.0	0.4	$\text{La}_2\text{Ni}_{0.6}\text{Cu}_{0.4}\text{O}_{4+\delta}$	[33]	70	2.23	LSGM
0.3	0.1	$\text{La}_{1.7}\text{Ca}_{0.3}\text{Ni}_{0.9}\text{Cu}_{0.1}\text{O}_{4+\delta}$	[37]	130	0.89	LSGM
0.3	0.2	$\text{La}_{1.7}\text{Ca}_{0.3}\text{Ni}_{0.8}\text{Cu}_{0.2}\text{O}_{4+\delta}$	[37]	145	0.79	LSGM
0.3	0.3	$\text{La}_{1.7}\text{Ca}_{0.3}\text{Ni}_{0.7}\text{Cu}_{0.3}\text{O}_{4+\delta}$	[37]	156	0.50	LSGM
0.3	0.25	$\text{La}_{1.7}\text{Ca}_{0.3}\text{Ni}_{0.75}\text{Cu}_{0.25}\text{O}_{4+\delta}$	[45]		0.50	YSZ
0.3	0.25	$\text{La}_{1.7}\text{Ca}_{0.3}\text{Ni}_{0.75}\text{Cu}_{0.25}\text{O}_{4+\delta}$	[43]		0.07	$\text{Ce}_{0.8}\text{Gd}_{0.2}\text{O}_{1.9}$
0.3	0.5	$\text{La}_{1.7}\text{Ca}_{0.3}\text{Ni}_{0.5}\text{Cu}_{0.5}\text{O}_{4+\delta}$	[45]		0.63	YSZ
0.3	0.75	$\text{La}_{1.7}\text{Ca}_{0.3}\text{Ni}_{0.25}\text{Cu}_{0.75}\text{O}_{4+\delta}$	[45]		1.95	YSZ
0.4	0.1	$\text{La}_{1.6}\text{Ca}_{0.4}\text{Ni}_{0.9}\text{Cu}_{0.1}\text{O}_{4+\delta}$	[46]	125		
0.4	0.2	$\text{La}_{1.6}\text{Ca}_{0.4}\text{Ni}_{0.8}\text{Cu}_{0.2}\text{O}_{4+\delta}$	[46]	103		
0.4	0.3	$\text{La}_{1.6}\text{Ca}_{0.4}\text{Ni}_{0.7}\text{Cu}_{0.3}\text{O}_{4+\delta}$	[46]	94		

In connection with the prospects of using the  $\text{La}_{1.7}\text{Ca}_{0.3}\text{Ni}_{1-y}\text{Cu}_y\text{O}_{4+\delta}$  oxides as cathode materials for IT-SOFCs and materials for MIEC membranes, it is of interest to study the correlation between the features of the crystal structure, electrical transport properties in air and under various oxygen partial pressure values, oxygen permeability, as well as their thermomechanical properties and electrochemical activity of the  $\text{La}_{1.7}\text{Ca}_{0.3}\text{Ni}_{1-y}\text{Cu}_y\text{O}_{4+\delta}$ -based electrodes in contact with the SDC electrolyte without/with a collector layer.

## 2. Materials and Methods

### 2.1. Synthesis of the Materials and Preparation of the Compact Samples

The  $\text{La}_{1.7}\text{Ca}_{0.3}\text{Ni}_{1-y}\text{Cu}_y\text{O}_{4+\delta}$  ( $y = 0.0\text{--}0.4$ ) samples were synthesized via a conventional solid-state reaction method. Starting materials  $\text{La}_2\text{O}_3$  (99.999% purity),  $\text{CaCO}_3$  (analytical grade, 99.4%),  $\text{NiO}$ , and  $\text{CuO}$  (analytical grade, 99.0%) were mixed and calcined at 1000 °C for 10 h. This was followed by milling in a planetary mill Fritsch Pulverizette 7 (Idar-Oberstein, Germany) with a rate of 250 rpm in isopropyl alcohol for 1 h in an agate drum with stainless steel milling media taken to the powder weight in the ratio of 5:1. Final synthesis was performed at 1200 °C for 10 h for the powders with  $y = 0.0\text{--}0.2$  and at 1150 °C for 10 h for the powders with  $y = 0.3\text{--}0.4$ . The specific surface area of the powders was determined after the final milling for 1 h and drying by means of a META SORBI N.4.1

analyzer (Moscow, Russia) was in a range of 0.94–1.16 m<sup>2</sup>·g<sup>-1</sup>. The impurity content in the as-prepared powders caused by milling was determined by an inductively coupled plasma optical emission spectrometry (ICP-OES) using a Perkin Elmer OPTIMA 4300 DV device (Waltham, MA, USA) and amounted to approximately 0.3 (Fe) and 0.4 (Si) wt. % (Supplementary Data, Table S1). Additionally, impurity content was determined using SEM analysis, performed by means of a Tescan VEGA 3 scanning electron microscope equipped with an Ultim Max 40 detector (Brno – Kohoutovice, Czech Republic). The amount of impurities was in a range of 0.4–0.5 (Fe) and 0.4–0.7 (Si) wt. % (Supplementary Data, Table S1, Figures S1–S3).

For the preparation of dense ceramics, the synthesized La<sub>1.7</sub>Ca<sub>0.3</sub>Ni<sub>1-y</sub>Cu<sub>y</sub>O<sub>4+δ</sub> (y = 0.0–0.4) powders were compacted uniaxially at 40 MPa into disk-shaped pellets (diameter 18 mm, thickness 1.5–2.0 mm). This was followed by isostatic pressing (200 Mpa) and annealing in air at various temperatures depending on Cu content (Table 3). The experimental density of the sintered ceramics (Table 3) was calculated from the sample weight and geometric dimensions of the polished disk-shaped samples. The rectangular bars for the dilatometric and electrical measurements were cut out of the disk-shaped samples using a Struers Minitom precision cutting machine (Copenhagen, Denmark) with a diamond cutoff disk.

**Table 3.** Tolerance factors, refined structural parameters, and absolute oxygen non-stoichiometry values for the La<sub>1.7</sub>Ca<sub>0.3</sub>Ni<sub>1-y</sub>Cu<sub>y</sub>O<sub>4+δ</sub> series.

	y	0.0	0.1	0.2	0.3	0.4
	<i>t</i>	0.895	0.893	0.891	0.890	0.888
	<i>a</i> , Å	3.829(1)	3.824(1)	3.820(1)	3.810(1)	3.803(1)
	<i>c</i> , Å	12.598(1)	12.644(1)	12.676(1)	12.758(1)	12.804(1)
	<i>V</i> , Å <sup>3</sup>	184.689(9)	184.863(9)	184.975(9)	185.236(9)	185.206(7)
	ρ <sub>XRD</sub> , g·cm <sup>-3</sup>	6.682	6.673	6.678	6.677	6.690
	<i>z</i> (La/Ca)	0.362(1)	0.362(1)	0.362(1)	0.362(1)	0.362(1)
	<i>z</i> (O2)	0.174(1)	0.176(1)	0.176(1)	0.177(1)	0.177(1)
	La/Ca-La/Ca	3.480(2)	3.491(2)	3.502(2)	3.519(2)	3.534(2)
	Ni/Cu-La/Ca	3.218(1)	3.218(1)	3.219(1)	3.219(1)	3.218(1)
	Ni/Cu-Ni/Cu	3.829(1)	3.824(1)	3.820(1)	3.810(1)	3.803(1)
L, Å	Ni/Cu-O1x4	1.914(1)	1.912(1)	1.909(1)	1.905(1)	1.902(1)
	Ni/Cu-O2x2	2.202(9)	2.219(9)	2.234(9)	2.249(8)	2.261(8)
	La/Ca-O1x4	2.587(1)	2.589(1)	2.591(1)	2.593(1)	2.596(1)
	La/Ca-O2x4	2.745(2)	2.745(2)	2.743(2)	2.739(2)	2.734(2)
	La/Ca-O2x1	2.350(9)	2.357(9)	2.361(9)	2.371(8)	2.374(8)
	R <sub>Br</sub>	2.88	2.63	6.17	2.57	3.94
	R <sub>f</sub>	2.39	1.98	3.79	1.62	2.10
	R <sub>exp</sub>	4.27	4.28	4.82	5.36	5.35
	R <sub>wp</sub>	10.5	10.00	11.6	10.1	10.1
	R <sub>p</sub>	8.03	7.28	8.80	7.78	7.79
	χ <sup>2</sup>	6.01	5.55	5.79	3.53	3.56
	δ <sub>TGA</sub>	0.05(1)	0.01(1)	0.01(1)	0.00(1)	0.01(1)
	T <sub>sintering</sub> , °C	1450	1415	1380	1340	1300
	ρ, g cm <sup>-3</sup>	6.44	6.52	6.57	6.39	6.51
	Relative density, %	96.4	97.7	98.3	95.7	97.3

### 2.2. X-ray Diffraction Analysis and Crystal Structure Refinement

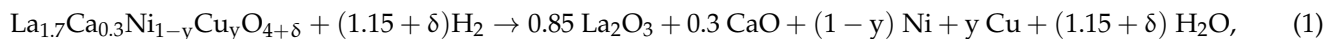
The powder X-ray diffraction experiments, necessary for the determination of the phase purity of the La<sub>1.7</sub>Ca<sub>0.3</sub>Ni<sub>1-y</sub>Cu<sub>y</sub>O<sub>4+δ</sub> (y = 0.0–0.4) samples and their crystal structure refinement, were performed using a Shimadzu XRD-7000 diffractometer (Tokyo, Japan) with a graphite monochromator in CuKα<sub>1</sub> radiation at 25 °C in air. X-ray diffraction patterns were obtained over an angle range of 25 < 2θ < 80 with a step of 0.02° and an exposition of 5 s per step. The structure refinement in the La<sub>1.7</sub>Ca<sub>0.3</sub>Ni<sub>1-y</sub>Cu<sub>y</sub>O<sub>4+δ</sub>

series was performed via the Rietveld full-profile analysis method using the FullProf Suite program package [47].

The powder X-ray diffraction data, necessary to qualify the SDC and LNF phase purity, were obtained on a DRON 6 diffractometer (Saint Petersburg, Russia) with a graphite monochromator in  $\text{CuK}\alpha_1$  radiation at 25 °C in air. X-ray patterns were collected over an angle range of  $25 < 2\theta < 80$  with a step of  $0.04^\circ$  and an exposition of 1 s per step.

### 2.3. Oxygen Nonstoichiometry Study

The room-temperature values of the absolute oxygen non-stoichiometry ( $\delta$ ) in the  $\text{La}_{1.7}\text{Ca}_{0.3}\text{Ni}_{1-y}\text{Cu}_y\text{O}_{4+\delta}$  ( $y = 0.0\text{--}0.4$ ) series were determined from the weight loss detected by the thermogravimetric analysis during the full reduction in a hydrogen-containing atmosphere. This is a traditional method employed for the studies of oxygen non-stoichiometry in oxides with easily reducible transition metal cations (e.g., Refs. [32,36]). The experiments were performed using a NETZSCH STA 449 F3 Jupiter thermal analyzer (Stuttgart, Germany) on heating in a 50%  $\text{H}_2$ /50% Ar gas mixture from room temperature to 1000 °C at  $10^\circ\text{C min}^{-1}$ . The procedure resulted in a reduction of the complex oxide to a mixture of metallic nickel and copper co-existing with lanthanum and calcium oxides, as confirmed by the XRD analysis:



The value of  $\delta$  in the initial nickelate was calculated from the change in the weight of the sample as follows:

$$\delta = \left( \frac{m_0}{m_{\text{red}}} M_{\text{red}} - M_{\text{cat}} \right) / M_{\text{O}} - 4, \quad (2)$$

where  $m_0$  and  $m_{\text{red}}$  are the weight of the initial sample and the reduced sample, respectively,  $M_{\text{red}}$  is the molar mass of the reduced sample,  $M_{\text{cat}}$  is the molar mass of cations (taking the stoichiometry indexes into account), and  $M_{\text{O}}$  is the mass of one mole of oxygen atoms.

### 2.4. Scanning Electron Microscopy

Microstructural characterization of the sintered ceramic samples  $\text{La}_{1.7}\text{Ca}_{0.3}\text{Ni}_{1-y}\text{Cu}_y\text{O}_{4+\delta}$  ( $y = 0.0; 0.2; 0.4$ ) was performed using a Hitachi SU-70 microscope equipped with a Bruker Quantax 400 detector (Karlsruhe, Germany) for the energy dispersive spectroscopy (EDS) analysis. The microstructure and the chemical composition of the  $\text{La}_{1.7}\text{Ca}_{0.3}\text{Ni}_{1-y}\text{Cu}_y\text{O}_{4+\delta}$  ( $y = 0.0; 0.2; 0.4$ ) electrodes with/without the  $\text{LaNi}_{0.6}\text{Fe}_{0.4}\text{O}_{3-\delta}$  (LNF) collector layer in contact with the SDC electrolyte substrate were examined using a Tescan VEGA 3 scanning electron microscope equipped with an Ultim Max 40 detector (Brno-Kohoutovice, Czech Republic).

### 2.5. Investigation of the Electrical Properties and Oxygen Permeability

The electrical conductivity of the  $\text{La}_{1.7}\text{Ca}_{0.3}\text{Ni}_{1-y}\text{Cu}_y\text{O}_{4+\delta}$  ( $y = 0.0\text{--}0.4$ ) ceramic samples was measured by a DC four-probe method as a function of temperature (100–950 °C) in air and as a function of oxygen partial pressure at 800 °C in the  $p\text{O}_2$  range from  $\sim 10^{-5}$  to 1.0 atm. The platinum paste was applied onto the end-face surfaces of the rectangular bar-shaped samples to ensure uniform electrical contact. Pt wires were used as potential probes and current collectors. Oxygen partial pressure,  $p\text{O}_2$ , was regulated by the composition of the flowing  $\text{O}_2 + \text{N}_2$  gas mixture and controlled using an electrochemical yttria-stabilized zirconia (YSZ) oxygen sensor. The flow rates of the gases were set by means of Bronkhorst mass flow controllers (Ruurlo, the Netherlands).

Investigation of oxygen permeability through the  $\text{La}_{1.7}\text{Ca}_{0.3}\text{Ni}_{1-y}\text{Cu}_y\text{O}_{4+\delta}$  ( $y = 0.0; 0.4$ ) ceramic membranes was performed at 800–950 °C using electrochemical YSZ solid electrolyte cells comprising an oxygen pump and a sensor [48]. The gas-tight ceramic disks of 1 mm in thickness were preliminarily tested for the absence of physical leakages under the total pressure gradient of  $\sim 2$  atm (at 25 °C). Then, the disk was hermetically sealed onto the top of the YSZ electrochemical cell by a high-temperature glass sealant at 1100 °C.

The oxygen partial pressure at the membrane feed side ( $p_2$ ) was equal to 0.21 atm, while the  $p_{O_2}$  at the permeate side ( $p_1$ ) varied in the course of measurements using the YSZ cell electrochemical pump and was controlled by the YSZ cell electrochemical sensor.

### 2.6. Dilatometric Studies

Thermal expansion of the  $La_{1.7}Ca_{0.3}Ni_{1-y}Cu_yO_{4+\delta}$  ( $y = 0.0-0.4$ ) dense ceramics was studied by dilatometry using a vertical Linseis L75 instrument (Selb, Germany). The measurements were performed in the heating/cooling modes at the rate of  $3\text{ }^\circ\text{C}\cdot\text{min}^{-1}$  in flowing air between 25 and  $1100\text{ }^\circ\text{C}$ . The average thermal expansion coefficients (TECs) were calculated by linear approximation of the obtained dilatometric curves.

### 2.7. Electrode Polarization Resistance Experiments

The  $Ce_{0.8}Sm_{0.2}O_{1.9}$  (SDC) electrolyte substrates for the electrochemical measurements were fabricated from the powder obtained via a two-stage solid-state reaction route [34]. The material had a cubic fluorite-like structure (sp. gr.  $Fm3m$ ) with a unit cell parameter  $a = 5.5453(6)\text{ \AA}$ . The powder was dry-pressed and sintered in air at  $1620\text{ }^\circ\text{C}$  for 5 h. The substrates had a relative density of 95–97% and the thickness of approximately 1 mm.

The electrode slurries were fabricated by mixing the  $La_{1.7}Ca_{0.3}Ni_{1-y}Cu_yO_{4+\delta}$  ( $y = 0.0; 0.2; 0.4$ ) electrode powders with ethanol and a 5 wt. % alcohol solution of the polyvinyl butyral binder with stirring for 2 h in an agate mortar. The electrodes were developed as single- and two-layer structures. To fabricate a single-layer electrode, the  $La_{1.7}Ca_{0.3}Ni_{1-y}Cu_yO_{4+\delta}$  slurry was brush-painted symmetrically onto the opposite sides of the SDC substrates to produce the functional layers with a thickness of  $\sim 30\text{ }\mu\text{m}$ . The cells were sintered at  $900-1100\text{ }^\circ\text{C}$  for 2 h or at  $1200\text{ }^\circ\text{C}$  for 1 h. For the fabrication of two-layer electrodes, the LNF + 3 wt. % CuO current collector layer (thickness of 15, 30, or  $50\text{ }\mu\text{m}$ ) was deposited over the functional layer, pre-sintered at  $1000\text{ }^\circ\text{C}$ , and sintered at  $900\text{ }^\circ\text{C}$  for 2 h. The method of preparation of the current collector based on LNF with the CuO additive was developed earlier; the LNF powder was synthesized via a nitrate combustion method as described elsewhere [49]. The LNF had a rhombohedral perovskite structure (sp. gr.  $R-3c$ ) with unit cell parameters  $a = 5.506(1)$ ;  $c = 13.252(1)\text{ \AA}$ .

The electrode performance was investigated by electrochemical impedance spectroscopy (EIS) on the fabricated symmetric cells using an electrochemical station comprising an SI-1260 frequency analyzer (Solartron Analytical, Farnborough, UK) and an SI-1287 electrochemical interface (Solartron Analytical, Farnborough, UK). The measurements were performed in a frequency range of 0.01 Hz–0.5 MHz with an applied *ac* signal amplitude of 30 mV. The EIS spectra were collected in the temperature range of  $600-850\text{ }^\circ\text{C}$  with a step of  $50\text{ }^\circ\text{C}$  in air. Each measurement was followed by recording the total *dc* cell resistance ( $R_{dc}$ ). The distribution functions of relaxation times (DFRTs) were obtained by Tikhonov regularization (TR) in the MATLAB version of the DRTtools software [50,51]. The calculations were carried out using a Gaussian-type function with the regularization parameter (RP) of 0.001. The combined Re-Im data setting was chosen in the calculation process.

## 3. Results and Discussion

### 3.1. Structure and Oxygen Content in the $La_{1.7}Ca_{0.3}Ni_{1-y}Cu_yO_{4+\delta}$ Materials

The XRD data for the powdered samples indicated the existence of a  $La_{1.7}Ca_{0.3}Ni_{1-y}Cu_yO_{4+\delta}$  solid solution with a tetragonal structure. The results of the structural refinement of the XRD data obtained by a full-profile Rietveld analysis using the space group of  $I4/mmm$  are presented in Table 3. Crystal structure refinement was carried out according to the reference data for  $La_{1.7}Ca_{0.3}NiO_{4+\delta}$  (JCPDS PDF#79-9864), assuming a uniform distribution of lanthanum/calcium and nickel/copper atoms in the corresponding sublattices. The observed and calculated XRD patterns are shown in Figure 1a–e.

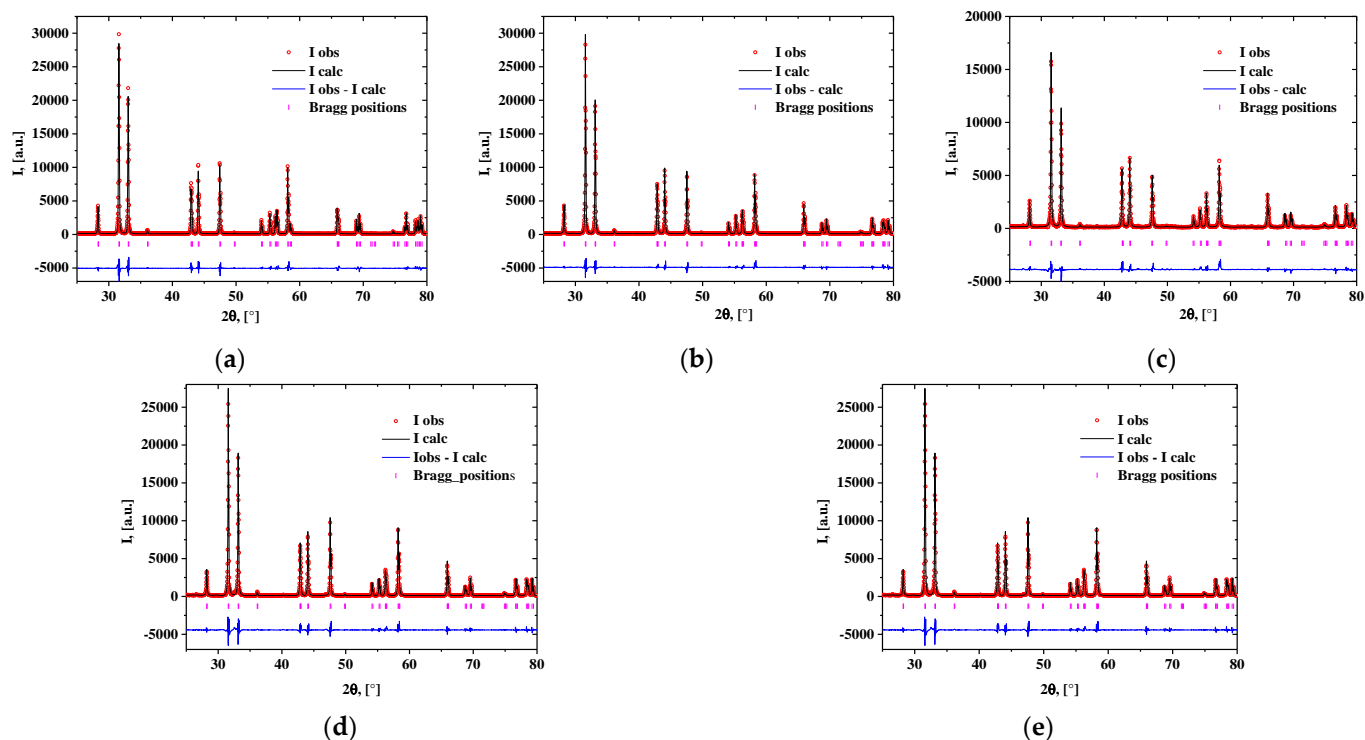


**Figure 1.** Observed (points) and calculated (lines) XRD patterns for the  $\text{La}_{1.7}\text{Ca}_{0.3}\text{Ni}_{1-y}\text{Cu}_y\text{O}_{4+\delta}$  powdered samples: (a)  $\text{La}_{1.7}\text{Ca}_{0.3}\text{NiO}_{4+\delta}$ ; (b)  $\text{La}_{1.7}\text{Ca}_{0.3}\text{Ni}_{0.9}\text{Cu}_{0.1}\text{O}_{4+\delta}$ ; (c)  $\text{La}_{1.7}\text{Ca}_{0.3}\text{Ni}_{0.8}\text{Cu}_{0.2}\text{O}_{4+\delta}$ ; (d)  $\text{La}_{1.7}\text{Ca}_{0.3}\text{Ni}_{0.7}\text{Cu}_{0.3}\text{O}_{4+\delta}$ ; (e)  $\text{La}_{1.7}\text{Ca}_{0.3}\text{Ni}_{0.6}\text{Cu}_{0.4}\text{O}_{4+\delta}$ .

As discussed in [52], the Goldschmidt tolerance factor,  $t$ , is a quantitative estimate of micro-strains in the  $\text{Ln}_2\text{NiO}_{4+\delta}$  structure due to a mismatch between the lattice parameters in the  $a,b$ -plane of the perovskite layers and the rock-salt-type layers [53]. The  $t$  values presented in Table 3 were calculated using the conventional equation presented elsewhere, for example in [24], and the data for ionic radii, reported in [54]. It was found that an increase in the copper content in the  $\text{La}_{1.7}\text{Ca}_{0.3}\text{Ni}_{1-y}\text{Cu}_y\text{O}_{4+\delta}$  series resulted in a minor decrease in the  $t$  values. This means that a partial replacement of nickel ions by larger copper ions in the studied series causes an expansion along the (Ni/Cu)O<sub>2</sub> layers, which, in turn, may increase the strain between the perovskite layers and the rock-salt-type layers.

Analysis of the concentration dependencies for the unit cell parameters and volumes presented in Figure 2 showed an increase in the  $c$  parameter and the unit cell volume. This was due to the difference in the ionic radii between nickel and copper cations [54]. However, the  $a$  parameter slightly decreased with an increase in the copper content. Similar behavior of the concentration dependencies of the unit cell parameters was observed earlier for  $\text{La}_2\text{Ni}_{1-y}\text{Cu}_y\text{O}_{4+\delta}$  [32,33],  $\text{La}_{1.7}\text{Ca}_{0.3}\text{Ni}_{1-y}\text{Cu}_y\text{O}_{4+\delta}$  [37,45,46],  $\text{Nd}_2\text{Ni}_{1-y}\text{Cu}_y\text{O}_{4+\delta}$  [55],  $\text{Nd}_{1.8}\text{Sr}_{0.2}\text{Ni}_{1-y}\text{Cu}_y\text{O}_{4+\delta}$  [56],  $\text{Nd}_{1.6}\text{Ca}_{0.4}\text{Ni}_{1-y}\text{Cu}_y\text{O}_{4+\delta}$  [57], and  $\text{Pr}_{1.7}\text{Sr}_{0.3}\text{Ni}_{1-y}\text{Cu}_y\text{O}_{4+\delta}$  [58].

The above-mentioned behavior of the concentration dependencies of the unit cell parameters for  $\text{La}_{1.7}\text{Ca}_{0.3}\text{Ni}_{1-y}\text{Cu}_y\text{O}_{4+\delta}$  may be explained by the Jahn–Teller effect of copper cations [32,59]. Copper cations are able to form elongated  $\text{CuO}_6$  octahedrons in place of more regular  $\text{NiO}_6$  ones, as can be seen from the pictures presented in Figure 3a with the selected bond lengths calculated by the Rietveld method. The observed results can be explained by the preference of  $\text{Cu}^{2+}$  cations for a square planar coordination [54], resulting in elongated Ni/Cu–O<sub>2</sub> bond length and shortened Ni/Cu–O<sub>1</sub> bond length (Supplementary Materials, Figure S4).

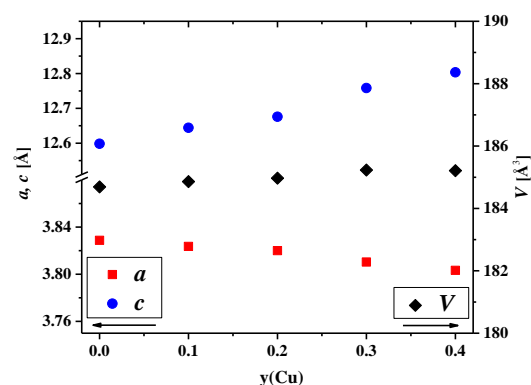


**Figure 2.** Dependencies of the unit cell parameters and volumes for the  $\text{La}_{1.7}\text{Ca}_{0.3}\text{Ni}_{1-y}\text{Cu}_y\text{O}_{4+\delta}$  series on the Cu content.

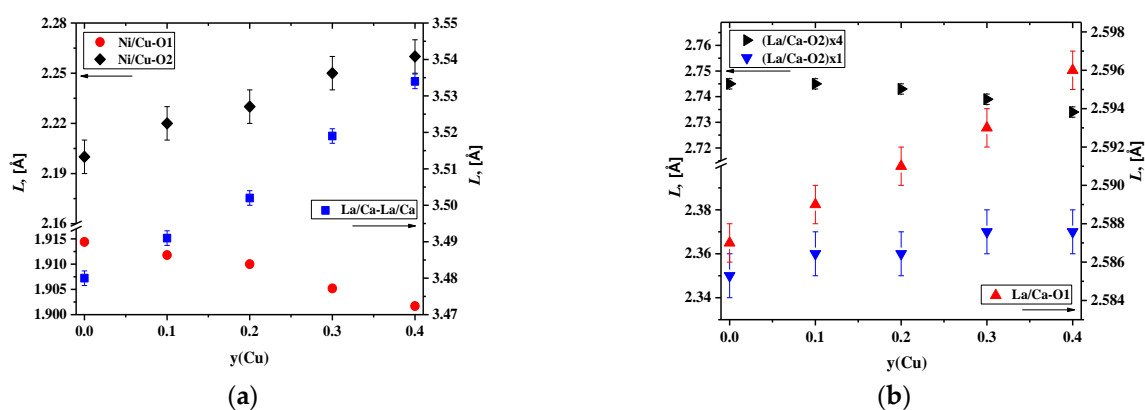


**Figure 3.** Interatomic distances in the  $\text{La}_{1.7}\text{Ca}_{0.3}\text{Ni}_{1-y}\text{Cu}_y\text{O}_{4+\delta}$  series in dependence on the Cu content: (a) Ni/Cu–O, and (b) La/Ca–La/Ca, La/Ca–O.

The data on the selected bond lengths presented in Table 3 and Figure 3a,b illustrate that the  $c$  parameter, equal to the sum of the doubled  $(\text{La}/\text{Ca}-\text{O}2)\times 1$ , doubled Ni/Cu–O2, and La/Ca–La/Ca distances, increases due to an increase in all the interatomic distances mentioned. The room-temperature values of the oxygen non-stoichiometry,  $\delta$ , for the  $\text{La}_{1.7}\text{Ca}_{0.3}\text{Ni}_{1-y}\text{Cu}_y\text{O}_{4+\delta}$  samples, calculated from the thermogravimetric data, are given in Table 3. It was found that the incorporation of copper cations into the nickel sublattice resulted in a drop in the absolute oxygen content. This can be explained by the preference of copper cations for a lower average oxidation state in isostructural oxide compounds compared to nickel cations, as evident, for instance, from the data on oxygen non-stoichiometry of  $\text{La}_2\text{CuO}_{4+\delta}$  [60] and  $\text{La}_2\text{NiO}_{4+\delta}$  [61] under identical  $p\text{O}_2$ - $T$  conditions. The changes in the oxygen content correlate with the tendency of the copper cations to create structures with a square planar coordination [46] and agree well with the literature data for the Cu-substituted samples:  $\text{La}_2\text{Ni}_{1-y}\text{Cu}_y\text{O}_{4+\delta}$  [62],  $\text{Nd}_2\text{Ni}_{1-y}\text{Cu}_y\text{O}_{4+\delta}$  [58],  $\text{La}_{1.6}\text{Ca}_{0.4}\text{Ni}_{1-y}\text{Cu}_y\text{O}_{4+\delta}$  [46],  $\text{La}_{1.5}\text{Pr}_{0.5}\text{Ni}_{1-y}\text{Cu}_y\text{O}_{4+\delta}$  [63],  $\text{Nd}_{1.5}\text{Pr}_{0.5}\text{Ni}_{1-y}\text{Cu}_y\text{O}_{4+\delta}$  [64], and  $\text{Nd}_{1.6}\text{Ca}_{0.4}\text{Ni}_{1-y}\text{Cu}_y\text{O}_{4+\delta}$  [57].

### 3.2. Electrical Conductivity

Figures 4a and S5 show that the electrical conductivity of  $\text{La}_{1.7}\text{Ca}_{0.3}\text{Ni}_{1-y}\text{Cu}_y\text{O}_{4+\delta}$  decreases with Cu content. The observed trend generally correlates with the literature data for the  $\text{La}_2\text{Ni}_{1-y}\text{Cu}_y\text{O}_{4+\delta}$  [32,33,59] and  $\text{La}_{1.6}\text{Ca}_{0.4}\text{Ni}_{1-y}\text{Cu}_y\text{O}_{4+\delta}$  [46] series. Taking into account the changes in the oxygen content (Table 3), the decrease in conductivity may be assigned to the reduction in the concentration of the electronic-charge-carriers—electron-holes localized on the B-site transition metal cations (i.e., the concentration of  $\text{Ni}^{3+}$ ).

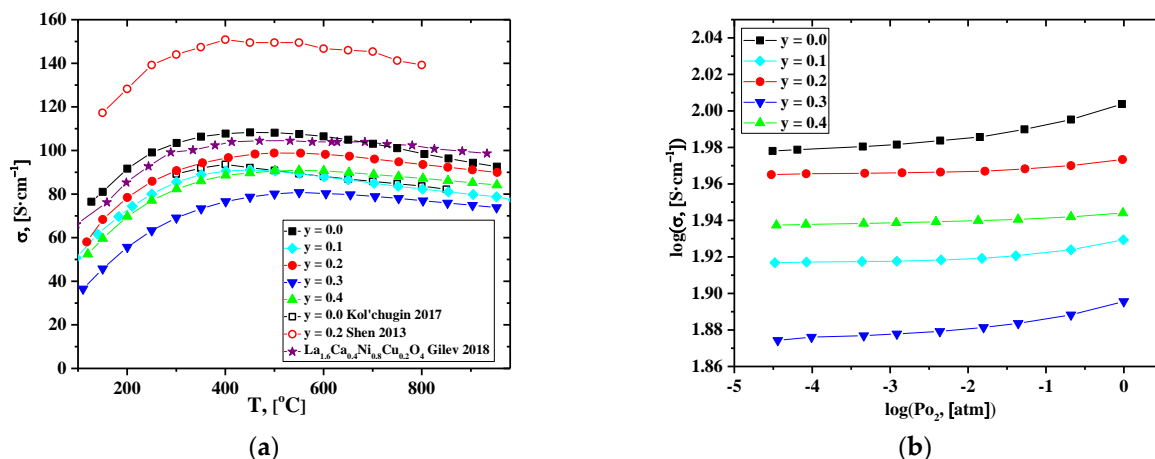
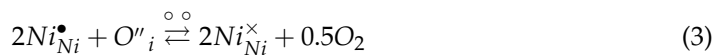


**Figure 4.** Dependencies of the total conductivity of the  $\text{La}_{1.7}\text{Ca}_{0.3}\text{Ni}_{1-y}\text{Cu}_y\text{O}_{4+\delta}$  ceramics on: (a) on temperature, and (b) on  $p\text{O}_2$  [35,37].

Shen et al. reported an increase in the total conductivity in the  $\text{La}_{1.7}\text{Ca}_{0.3}\text{Ni}_{1-y}\text{Cu}_y\text{O}_{4+\delta}$  series [37]. The authors supposed that it could be related to increasing the content of the interstitial oxygen in the samples. However, according to our data on the concentration dependence of  $\delta$  values, the interstitial oxygen content decreases with Cu-doping, at least at lower temperatures. A non-monotonous concentration dependence of the conductivity (Figure S5) and lower conductivity values compared to those presented in [37] may be related to the presence of the Si-containing impurities (most likely, in the form of inclusions of apatite-type  $\text{La}_{10-x}\text{Si}_6\text{O}_{26+\delta}$ -based phase [65]) in the samples as a result of contamination during the milling procedure (Figure S6). Additionally, it is worth noting that the  $\text{La}_{1.7}\text{Ca}_{0.3}\text{Ni}_{1-y}\text{Cu}_y\text{O}_{4+\delta}$  samples in [37] were synthesized by a citrate–nitrate combustion method, and the sintering temperatures were lower than those used in the present study; thus, the formation of secondary phases could be less significant compared to the solid-state reaction method. Available literature reports, including our results [66–68] and the works of other authors [69–72], confirm that the preparative route can be responsible for variations in the physicochemical properties of the complex oxides. In the future, we plan to find a more advanced synthesis procedure for this series. Nevertheless, it should be noted that the conductivity values obtained in this study (103, 96, and 89  $\text{S cm}^{-1}$  for  $y = 0.0, 0.2,$  and  $0.4$ , correspondingly, at  $T = 700\text{ °C}$ ) were close to those presented in [33–46] (Table 2).

Dependencies of the total conductivity on  $p\text{O}_2$  obtained for the  $\text{La}_{1.7}\text{Ca}_{0.3}\text{Ni}_{1-y}\text{Cu}_y\text{O}_{4+\delta}$  compact samples are presented in Figure 4b. As for parent  $\text{La}_2\text{NiO}_{4+\delta}$ , the conductivity slightly decreases with reducing  $p\text{O}_2$ , which can be related to the reversible oxygen losses from the oxide structure and reduction of Ni cations. This process can be described as follows:



The obtained data confirm that electronic transport in the studied materials is p-type.

### 3.3. Oxygen Permeability and Ionic Transport

The oxygen permeability of the copper-free  $\text{La}_{1.7}\text{Ca}_{0.3}\text{NiO}_{4+\delta}$  and  $\text{La}_{1.7}\text{Ca}_{0.3}\text{Ni}_{0.6}\text{Cu}_{0.4}\text{O}_{4+\delta}$  ceramics with the highest copper content was studied at 850–950 °C. Figure 5a demonstrates the dependence of the oxygen permeation fluxes through the  $\text{La}_{1.7}\text{Ca}_{0.3}\text{Ni}_{0.6}\text{Cu}_{0.4}\text{O}_{4+\delta}$  membrane on the oxygen partial pressure gradient in the studied temperature range, while Figure 5b compares the oxygen permeation fluxes through the undoped  $\text{La}_2\text{NiO}_{4+\delta}$  and  $\text{La}_{1.7}\text{Ca}_{0.3}\text{Ni}_{1-y}\text{Cu}_y\text{O}_{4+\delta}$  membranes under the fixed oxygen partial pressure gradient across the membranes. The results indicate that the calcium-substituted and copper-co-substituted oxides exhibit nearly three orders of magnitude lower oxygen permeability compared to

the parent lanthanum nickelate. This is accompanied by an increase in activation energy for oxygen permeation from 80 to 100 kJ/mol at 850–950 °C.

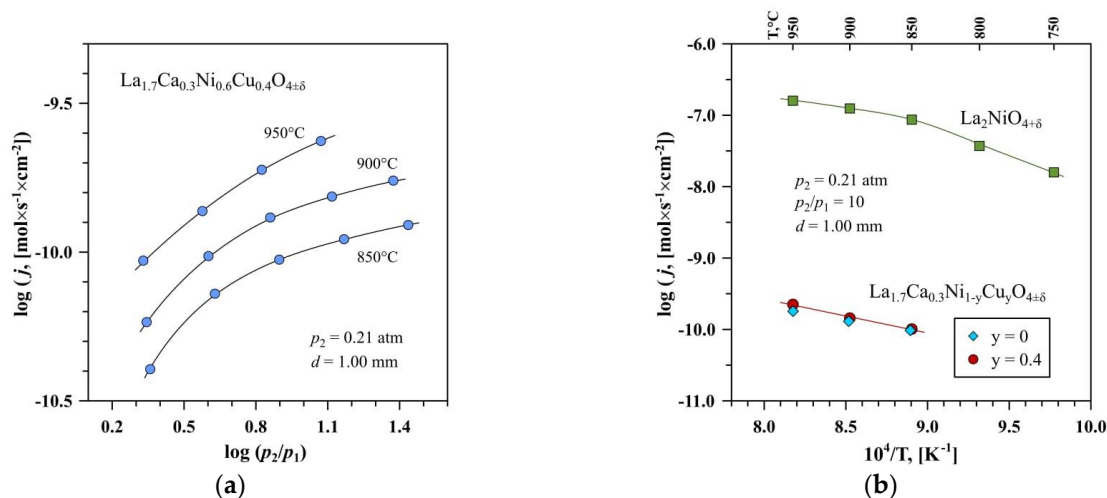


**Figure 5.** (a) Dependencies of the oxygen permeation fluxes through the La<sub>1.7</sub>Ca<sub>0.3</sub>Ni<sub>0.6</sub>Cu<sub>0.4</sub>O<sub>4+δ</sub> ceramic membrane on the  $p_{O_2}$  gradient at 850–950 °C, and (b) Temperature dependences of the oxygen permeation fluxes through the La<sub>1.7</sub>Ca<sub>0.3</sub>Ni<sub>0.6</sub>Cu<sub>0.4</sub>O<sub>4+δ</sub> and La<sub>1.7</sub>Ca<sub>0.3</sub>NiO<sub>4+δ</sub> membranes under the fixed  $p_{O_2}$  gradient. The data on the undoped La<sub>2</sub>NiO<sub>4+δ</sub> sample are taken from [65].

The suppression of oxygen ionic transport in La<sub>1.7</sub>Ca<sub>0.3</sub>Ni<sub>1-y</sub>Cu<sub>y</sub>O<sub>4+δ</sub> should be attributed mainly to the decrease in the concentration of mobile oxygen ions caused by the acceptor-type substitution of La<sup>3+</sup> by Ca<sup>2+</sup>. In particular, oxygen non-stoichiometry  $\delta$  in La<sub>1.7</sub>Ca<sub>0.3</sub>Ni<sub>1-y</sub>Cu<sub>y</sub>O<sub>4+δ</sub> corresponds to 0.01–0.05 at room temperature (Table 3) and is expected to tend to zero for both compositions at 850–950 °C under atmospheric oxygen pressure, by analogy with La<sub>2-x</sub>Sr<sub>x</sub>NiO<sub>4+δ</sub> ( $x = 0.2$ – $0.4$ ) nickelates [24,73]. As a result, oxygen permeability through the La<sub>1.7</sub>Ca<sub>0.3</sub>Ni<sub>1-y</sub>Cu<sub>y</sub>O<sub>4+δ</sub> membranes is nearly independent on the copper content, within the limit of experimental uncertainty. On the contrary, oxygen excess in La<sub>2</sub>NiO<sub>4+δ</sub> varies between  $\delta = 0.15$  at room temperature and  $\sim 0.08$  at 950 °C [61,67]. Generally, the obtained results agree well with the literature data on the La<sub>2-x</sub>Ca<sub>x</sub>NiO<sub>4+δ</sub> system indicating a decrease in oxygen diffusion and surface exchange coefficients with calcium doping and an increase in the corresponding activation energies [74,75].

One should also note that silica-based impurities may have negative effects on both bulk ionic transport and surface exchange kinetics. However, comparing the results on the oxygen permeability obtained in the present work with the data for silica-contaminated La<sub>2</sub>NiO<sub>4+δ</sub> [65], one may conclude that the role of impurities is relatively insignificant compared to the effects induced by the acceptor-type substitution. Oxygen-ionic conductivity in mixed ionic-electronic conductors can be roughly estimated from the data on oxygen permeability and total electrical conductivity using the Wagner equation for the steady-state oxygen permeation flux density through the membrane bulk and neglecting surface exchange limitations (e.g., Ref. [67]). The calculations showed that the oxygen-ionic conductivity,  $\sigma_O$ , in La<sub>1.7</sub>Ca<sub>0.3</sub>Ni<sub>1-y</sub>Cu<sub>y</sub>O<sub>4+δ</sub> at 850–950 °C was six orders of magnitude lower than electronic conductivity. The estimated values of  $\sigma_O$  corresponded to  $1.5 \times 10^{-4}$  S/cm at 950 °C and decreased on cooling, being nearly independent of copper content.

### 3.4. Thermomechanical Properties

Dilatometry experiments were performed both in heating and cooling modes. As an example, the temperature dependencies of the linear expansion of the La<sub>1.7</sub>Ca<sub>0.3</sub>Ni<sub>1-y</sub>Cu<sub>y</sub>O<sub>4+δ</sub> compact samples collected in air during heating are shown in Figure 6. Based on the obtained experimental data, the averaged values of the La<sub>1.7</sub>Ca<sub>0.3</sub>Ni<sub>1-y</sub>Cu<sub>y</sub>O<sub>4+δ</sub> linear thermal expansion coefficients (TECs) in the studied temperature range of 40–1100 °C were calculated and compared with the data presented in the literature (Table 4).

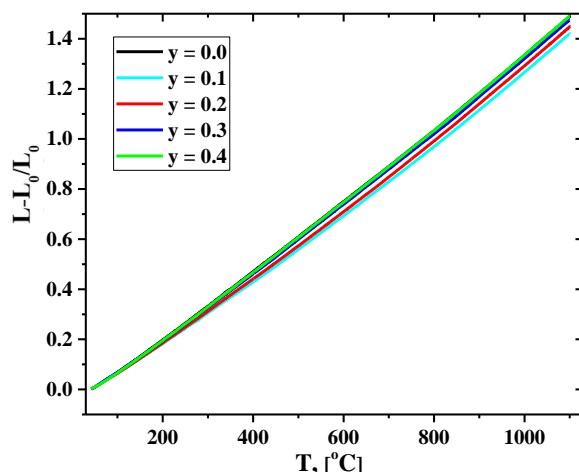


**Figure 6.** Temperature dependencies of the relative elongation of the  $\text{La}_{1.7}\text{Ca}_{0.3}\text{Ni}_{1-y}\text{Cu}_y\text{O}_{4+\delta}$  ceramic samples collected in a heating mode.

**Table 4.** Average TEC values for the  $\text{La}_{1.7}\text{Ca}_{0.3}\text{Ni}_{1-y}\text{Cu}_y\text{O}_{4+\delta}$  ceramics and other Cu- and Ca-substituted  $\text{La}_2\text{NiO}_{4+\delta}$  derivatives.

Sample	Ref.	T Range, °C	TEC × 10 <sup>6</sup> , K <sup>-1</sup>		
			Heating	Average Value	
				Heating	Cooling
y = 0.0	This work	40–300	13.0(1)		
		300–800	14.0(1)		
		800–1100	15.2(1)		
		40–1100		14.1(1)	13.9(1)
y = 0.1	This work	40–300	11.8(1)		
		300–800	13.3(1)		
		800–1100	15.1(1)		
		40–1100		13.4(1)	13.1(1)
y = 0.2	This work	40–300	12.2(1)		
		300–800	13.6(1)		
		800–1100	15.2(1)		
		40–1100		13.7(1)	13.4(1)
y = 0.3	This work	40–300	12.7(1)		
		300–800	13.9(1)		
		800–1100	15.2(1)		
		40–1100		14.0(1)	13.8(1)
y = 0.4	This work	40–300	12.9(1)		
		300–800	14.1(1)		
		800–1100	15.3(1)		
		40–1100		14.2(1)	13.9(1)
$\text{La}_2\text{Ni}_{0.8}\text{Cu}_{0.2}\text{O}_{4-\delta}$	[33]	50–1000		13.9	
$\text{La}_2\text{Ni}_{0.8}\text{Cu}_{0.2}\text{O}_{4-\delta}$	[76]	100–980		14.2	
$\text{La}_2\text{Ni}_{0.6}\text{Cu}_{0.4}\text{O}_{4-\delta}$	[33]	50–1000		13.0	
$\text{La}_{1.7}\text{Ca}_{0.3}\text{Ni}_{0.75}\text{Cu}_{0.25}\text{O}_{4-\delta}$	[45]	50–850		14.4	
$\text{La}_{1.6}\text{Ca}_{0.4}\text{Ni}_{0.9}\text{Cu}_{0.1}\text{O}_{4+\delta}$	[46]	25–1000		14.9	
SDC	[77]	350–900		12.3	

The average TECs of the  $\text{La}_{1.7}\text{Ca}_{0.3}\text{Ni}_{1-y}\text{Cu}_y\text{O}_{4+\delta}$  ceramics at 40–1100 °C varied in a narrow range of  $(13.1\text{--}14.2) \times 10^{-6} \text{ K}^{-1}$ . For Cu-substituted compositions, a minor increase in the TEC value with an increase in the copper content seemed to correlate with the variations in the unit cell volume (Table 3). Noteworthy, the TEC values of the present study are

in good agreement with those obtained in the previous investigations of thermal expansion of the Cu-substituted  $\text{La}_{2-x}\text{Ca}_x\text{NiO}_{4+\delta}$  derivatives (Table 4). Additionally, the obtained data demonstrate that  $\text{La}_{1.7}\text{Ca}_{0.3}\text{Ni}_{1-y}\text{Cu}_y\text{O}_{4+\delta}$  and Sm-doped ceria solid-state electrolytes (SDC), chosen for the electrochemical studies, are thermo-mechanically compatible.

### 3.5. Microstructure and Chemical Composition of the $\text{La}_{1.7}\text{Ca}_{0.3}\text{Ni}_{1-y}\text{Cu}_y\text{O}_{4+\delta}$ -Based Cathodes

The morphology of the  $\text{La}_{1.7}\text{Ca}_{0.3}\text{Ni}_{0.6}\text{Cu}_{0.4}\text{O}_{4+\delta}$ /SDC cathode layers sintered at 1000 °C was investigated using SEM. The corresponding micrographs presented in Figure 7a–c show that the resulting layers exhibit uniform grain distribution and high porosity. The SEM data also demonstrate that there are no cracks or delamination at the single-layer  $\text{La}_{1.7}\text{Ca}_{0.3}\text{Ni}_{1-y}\text{Cu}_y\text{O}_{4+\delta}$ /SDC and the two-layer LNF/ $\text{La}_{1.7}\text{Ca}_{0.3}\text{Ni}_{1-y}\text{Cu}_y\text{O}_{4+\delta}$ /SDC interfaces, as it can be seen from Figure 7c,d. After sintering, the thickness of the functional layers decreased and was in the range of 18–27 µm in dependence of the sintering temperature and sinterability of the electrode material. Despite the addition of a sintering additive (CuO), shrinkage of the collector layers sintered at 900 °C was less significant. As for example, the thickness of the LNF collector deposited with a thickness of 50 µm was evaluated from the SEM image as 47–48 µm. The average size of particles in the electrodes increased with increasing the copper content due to the better sintering ability of the Cu-containing materials (Figure S7). However, it varied within a narrow range of 0.4–1.1 µm.

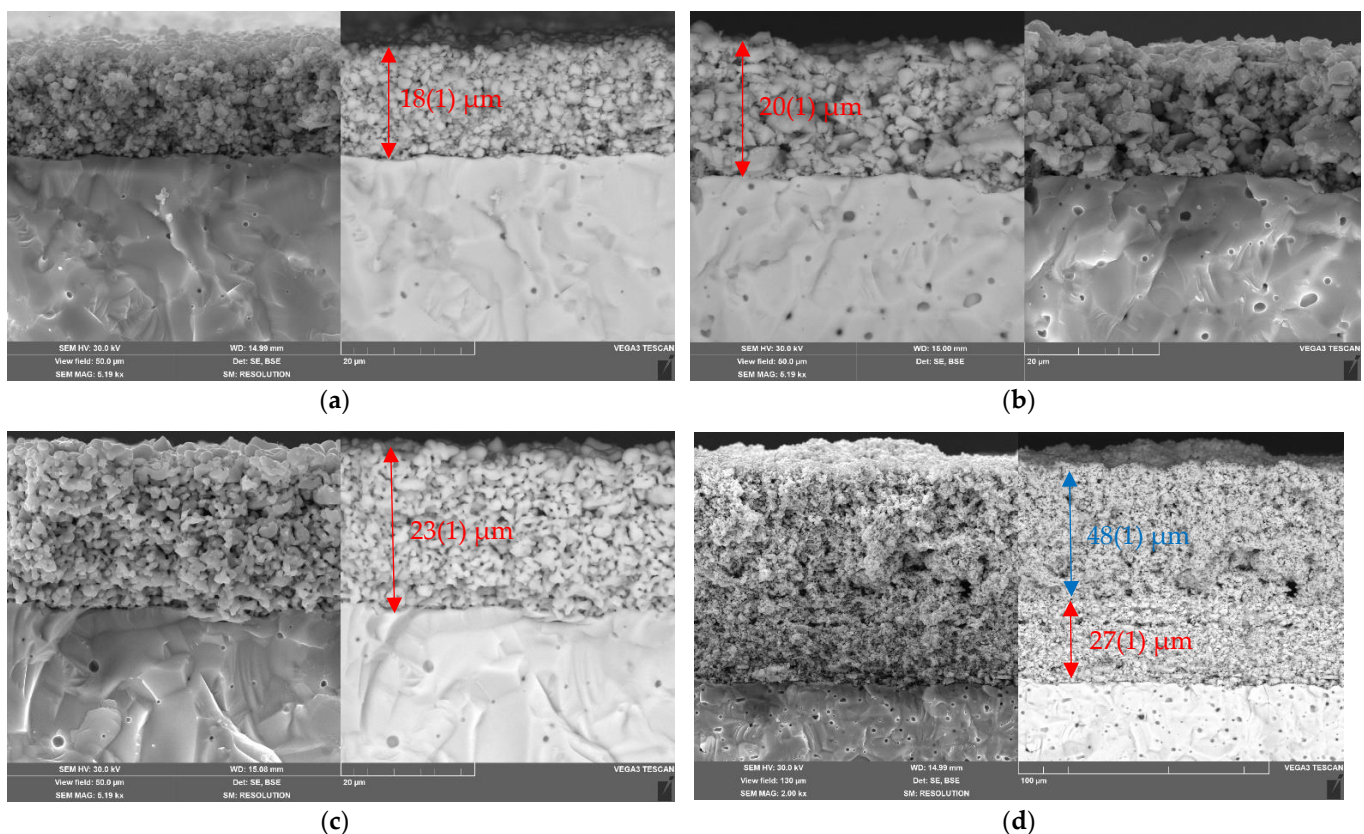


**Figure 7.** SEM images of the cross-sections of the  $\text{La}_{1.7}\text{Ca}_{0.3}\text{Ni}_{1-y}\text{Cu}_y\text{O}_{4+\delta}$ /SDC assemblies ( $T_s = 1000$  °C): (a) single-layer electrode  $y = 0.0$ ; (b) single-layer electrode  $y = 0.2$ ; (c) single-layer electrode  $y = 0.4$ ; (d) two-layer electrode  $y = 0.4$  ( $T_s = 900$  °C) with the LNF collector layer (50 µm,  $T_s = 900$  °C). The thickness of the  $\text{La}_{1.7}\text{Ca}_{0.3}\text{Ni}_{1-y}\text{Cu}_y\text{O}_{4+\delta}$  functional layers is shown in red, the thickness of the LNF collector is shown in blue.

The elemental distribution maps obtained by SEM/EDS for the  $\text{La}_{1.7}\text{Ca}_{0.3}\text{Ni}_{1-y}\text{Cu}_y\text{O}_{4+\delta}$  ( $y = 0.0; 0.2; 0.4$ ) electrode surface sintered at 1000 °C are shown in Figures S8–S10. The elemental compositions of the  $\text{La}_{1.7}\text{Ca}_{0.3}\text{Ni}_{1-y}\text{Cu}_y\text{O}_{4+\delta}$  electrodes (Table S3) were found to be close to the nominal, within the accuracy of the EDS technique. The data show that the

content of Si and Fe impurities in the sintered  $\text{La}_{1.7}\text{Ca}_{0.3}\text{Ni}_{1-y}\text{Cu}_y\text{O}_{4+\delta}$  electrodes were in the range of 2.00–2.45 and 0.80–1.11 at. %, correspondingly. These values obtained for the impurities are higher than those (Table S2) obtained for the as-prepared materials, probably, due to additional mechanical treatments during the electrode slurry preparation. In addition, impurities of light-weight elements can diffuse towards the surface of the samples during sintering of the electrodes, which can also be a possible reason for their increased content on the surface of the electrodes.

### 3.6. Electrochemical Studies

The influence of the sintering temperature of the electrode layers on the polarization characteristics was evaluated in preliminary electrochemical experiments (Figure S11). It can be seen that the optimal sintering temperature decreases with Cu substitution by 300 °C for the sample with  $y = 0.4$  (900 °C) compared to the copper-free  $\text{La}_{1.7}\text{Ca}_{0.3}\text{NiO}_{4+\delta}$  electrode (1200 °C). The preliminary studies also revealed that the polarization resistance of the copper-substituted  $\text{La}_{1.7}\text{Ca}_{0.3}\text{Ni}_{0.6}\text{Cu}_{0.4}\text{O}_{4+\delta}$  electrodes was lower than that of the parent material. To elucidate the impact of Cu substitution, a comprehensive analysis of the EIS data was performed. The impedance spectra for the  $\text{La}_{1.7}\text{Ca}_{0.3}\text{Ni}_{1-y}\text{Cu}_y\text{O}_{4+\delta}$ /SDC symmetrical cells ( $T_S = 1000$  °C) collected at 600 °C are shown in Figure 8a,b. The complex shape of the spectrum in Figure 8a indicates the presence of several contributions to the overall polarization resistance ( $R_p$ ). A comparison of the impedance plots measured at 600 °C in Figure 8b demonstrates that the polarization resistance of the studied cells significantly decreases when  $y \geq 0.3$ .

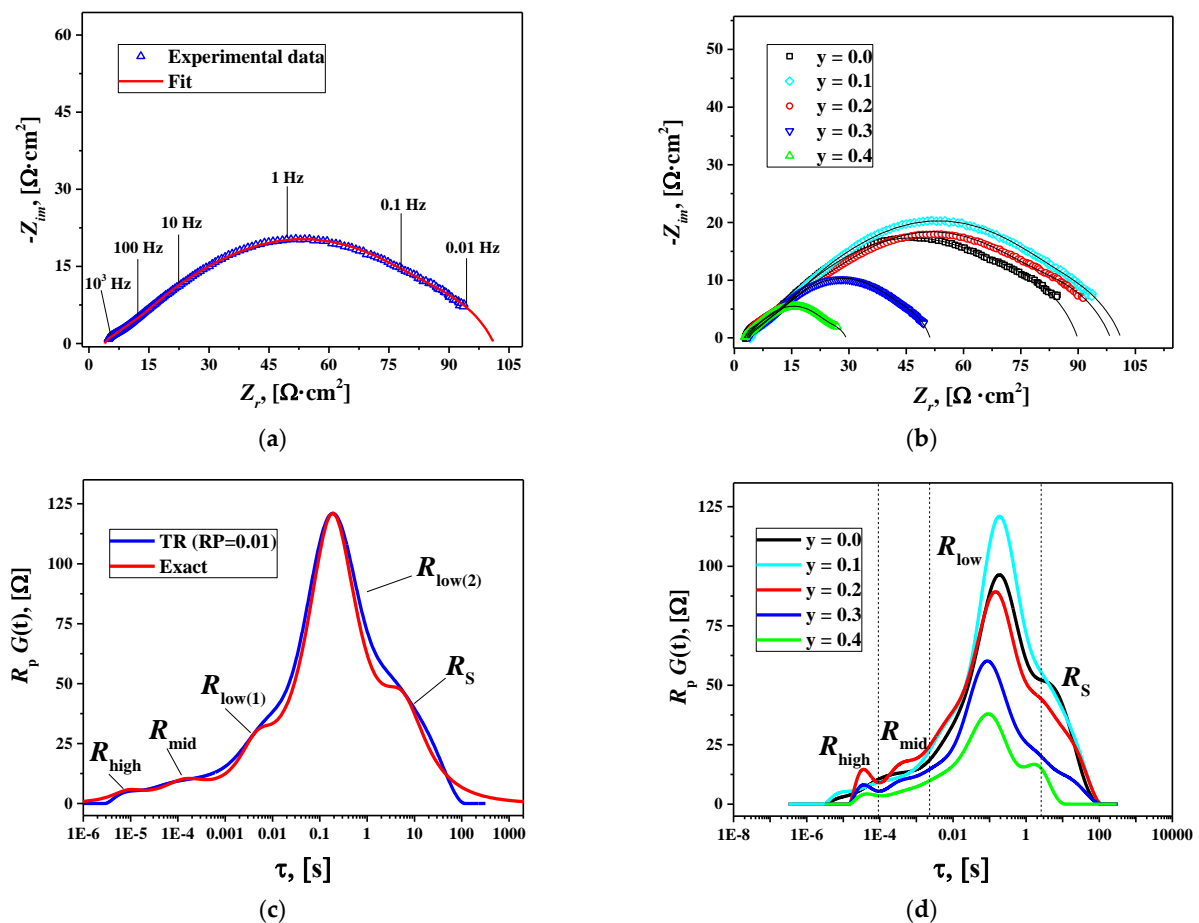


**Figure 8.** Fitted impedance spectra at 600 °C for the symmetrical cells: (a)  $\text{La}_{1.7}\text{Ca}_{0.3}\text{Ni}_{0.9}\text{Cu}_{0.1}\text{O}_{4+\delta}$ /SDC and (b)  $\text{La}_{1.7}\text{Ca}_{0.3}\text{Ni}_{1-y}\text{Cu}_y\text{O}_{4+\delta}$ /SDC; DFRTs at 600 °C for the symmetrical cells; (c)  $\text{La}_{1.7}\text{Ca}_{0.3}\text{Ni}_{0.9}\text{Cu}_{0.1}\text{O}_{4+\delta}$ /SDC, and (d)  $\text{La}_{1.7}\text{Ca}_{0.3}\text{Ni}_{1-y}\text{Cu}_y\text{O}_{4+\delta}$ /SDC.

The distribution functions of relaxation times (DFRTs) for the obtained impedance data were calculated using Tikhonov regularization (TR) in DRTtools [50,51]. A Gaussian-type function and a regularization parameter (RP) of 0.01 were used for calculations. The obtained DFRTs are shown in Figure 8c,d. The curves demonstrate the presence of at least five contributions to the polarization resistance of the  $\text{La}_{1.7}\text{Ca}_{0.3}\text{Ni}_{1-y}\text{Cu}_y\text{O}_{4+\delta}$ /SDC cells. One can observe two relatively small peaks at high ( $R_{\text{high}}$ ) and middle ( $R_{\text{mid}}$ ) frequencies and three significantly larger overlapping peaks at low frequencies ( $R_{\text{low}(1)}$ ,  $R_{\text{low}(2)}$ , and  $R_S$ ), which show that low-frequency processes dominate the polarization resistance of the studied cells. The  $R_{\text{low}(1)}$  and  $R_{\text{low}(2)}$  peaks merge into one peak ( $R_{\text{low}}$ ) at  $T > 650$  °C. Consequently, the  $R_{\text{low}(1)}$  and  $R_{\text{low}(2)}$  resistances can be determined as distinct values only at lower temperatures ( $T = 600$  °C). According to this, the equivalent circuit for fitting the impedance spectra consisted of ohmic resistance of the electrolyte  $R_0$  and four ( $T \geq 650$  °C) or five ( $T = 600$  °C)  $R$ - $CPE$  elements connected in series. The  $R$ - $CPE$  element, also known in the literature as ZARC, is a parallel combination of resistance and constant phase element. As an example, Figure 8a shows a satisfactory fit of the impedance spectrum for the  $\text{La}_{1.7}\text{Ca}_{0.3}\text{Ni}_{0.9}\text{Cu}_{0.1}\text{O}_{4+\delta}$ /SDC cell at 600 °C. The obtained fitting parameters were used to calculate the simulated DFRTs. For a ZARC, the simulated representation in  $\tau$ -space is the following [78,79]:

$$R \cdot G(\tau) = \frac{R}{2\pi} \cdot \frac{\sin[(1-n)\pi]}{\cosh[n \ln(\tau/\tau_0)] - \cos[(1-n)\pi]} \tag{4}$$

where  $\tau_0 = \sqrt[n]{R \cdot Q}$  is a time constant of the  $R$ - $CPE$  element, while  $Q$  and  $n$  are the pseudo-capacitance and the associated exponent of the angular frequency in  $Z_{CPE} = Q^{-1}(j\omega)^{-n}$ , respectively.

The simulated DFRT can be obtained as a sum of individual contributions:

$$R_p \cdot G(\tau) = \sum_i R_i \cdot G(\tau) \tag{5}$$

where  $R_p = \sum_i R_i$ .

Figure 8c compares the simulated DFRT and the one calculated by the TR method for the  $\text{La}_{1.7}\text{Ca}_{0.3}\text{Ni}_{0.9}\text{Cu}_{0.1}\text{O}_{4+\delta}$ /SDC cell at 600 °C. The agreement between the two curves suggests the reliability of the fitting results. Similar results were observed for other studied cells. The resulting resistances  $R_{\text{high}}$ ,  $R_{\text{mid}}$ ,  $R_{\text{low}}$ ,  $R_S$ , and  $R_p$  at different temperatures are presented in Figure 9.

For the identification of the processes characterized by the obtained resistances, the capacitances were calculated as follows [80]:

$$C_i = R_i \binom{1-n_i}{n_i} Q^{\frac{1}{n_i}} \tag{6}$$

In addition, activation energy ( $E_i$ ) for each process was determined from the slope of the corresponding  $\log R_i = f(1/T)$  dependencies (Table 5).

**Table 5.** Activation energies of the processes that contribute to the polarization resistance of the  $\text{La}_{1.7}\text{Ca}_{0.3}\text{Ni}_{1-y}\text{Cu}_y\text{O}_{4+\delta}$ /SDC symmetrical cells.

y	$E_{\text{high}}$ , eV	$E_{\text{mid}}$ , eV	$E_{\text{low}}$ , eV	$E_S$ , eV	$E_p$ , eV
0.0	$0.99 \pm 0.07$	$1.17 \pm 0.08$	$1.81 \pm 0.06$	$2.07 \pm 0.05$	$1.68 \pm 0.02$
0.1	$0.74 \pm 0.1$	$1.02 \pm 0.04$	$1.54 \pm 0.01$	$1.90 \pm 0.08$	$1.44 \pm 0.01$
0.2	$0.76 \pm 0.1$	$1.12 \pm 0.08$	$1.76 \pm 0.05$	$2.02 \pm 0.09$	$1.55 \pm 0.04$
0.3	$0.98 \pm 0.03$	$1.02 \pm 0.07$	$1.54 \pm 0.04$	$1.82 \pm 0.09$	$1.43 \pm 0.03$
0.4	$0.97 \pm 0.07$	$0.75 \pm 0.09$	$1.65 \pm 0.09$	$1.70 \pm 0.1$	$1.38 \pm 0.05$

The high-frequency and middle-frequency processes have capacitances near  $10^{-6}$  and  $10^{-4}$  F  $\text{cm}^{-2}$ , respectively, and activation energies close to 1 eV, indicating that the  $R_{\text{high}}$

and  $R_{\text{mid}}$  resistances characterize interfacial charge transfer. Particularly, the  $R_{\text{high}}$  values can be associated with charge transfer through the electrolyte/electrode interface [81,82], while those of  $R_{\text{mid}}$  represent the charge transfer in the electrode or at the electrode/current collector interface [83–85]. For the low-frequency processes, the  $C_{\text{low}(1)}$ ,  $C_{\text{low}(2)}$ , and  $C_{\text{S}}$  capacitances vary in ranges of  $10^{-4}$ – $10^{-3}$ ,  $1$ – $4 \times 10^{-3}$ , and  $10^{-1}$ – $1$  F cm $^{-2}$ , respectively. These values are higher than typical double-layer capacitances and can be identified as “chemical” capacitances associated with changes in oxygen non-stoichiometry in the mixed conductor [81,86].

Taking into account the obtained capacitances and  $E_{\text{low}}$  activation energies, one can suggest that  $R_{\text{low}}$  resistances describe oxygen solid-state diffusion ( $R_{\text{low}(1)}$ ) and surface oxygen exchange ( $R_{\text{low}(2)}$ ) in the electrode material [81,84,85]. Larger  $C_{\text{S}}$  capacitances up to 1 F cm $^{-2}$  and even lower frequencies for the  $R_{\text{S}}$  contribution compared to those for  $R_{\text{low}}$  imply that the former is related to the oxygen gas-phase diffusion in the pores of the electrodes [86]. However, significant activation energy ( $E_{\text{S}}$ ) suggests that the  $R_{\text{S}}$  resistances can be associated with a more complex process that includes not only oxygen gas-phase diffusion but also oxygen exchange at the electrode/gas-phase interface.

A comparison of the obtained resistances in Figure 9 shows that the  $R_{\text{low}} = R_{\text{low}(1)} + R_{\text{low}(2)}$  resistances (i.e., solid-state diffusion and surface exchange) make the most significant contribution to the total polarization resistance of the studied cells in the temperature range of 600–800 °C. However, the relative contribution of charge transfer processes ( $R_{\text{high}}$  and  $R_{\text{mid}}$ ) to the resulting  $R_{\text{p}}$  values noticeably increases at higher temperatures, and for some studied cells, it becomes predominant at 850 °C.

The increase in copper content in  $\text{La}_{1.7}\text{Ca}_{0.3}\text{Ni}_{1-y}\text{Cu}_y\text{O}_{4+\delta}$  up to  $y = 0.2$  has little effect on the polarization resistance of the studied cells, as seen in Figure 9f. At  $y \geq 0.3$ , the  $R_{\text{low}}$  and  $R_{\text{S}}$  values decrease with increasing  $y$  leading to a reduction in the total polarization resistance. According to the results of the oxygen permeation study (Section 3.3), the Cu-doping shows an insignificant influence on the level of ionic conductivity, which is approximately the same for the first ( $x = 0.0$ ) and the last ( $x = 0.4$ ) member of the series. Boehm et al. reported that oxygen diffusion coefficients slightly decreased with copper doping in  $\text{La}_2\text{Ni}_{1-x}\text{Cu}_x\text{O}_{4+\delta}$  while the concentration of interstitial oxygen gradually decreased from 0.16 at  $x = 0$  down to 0.01 at  $x = 1$  [62]. However, copper substitution can facilitate the surface oxygen exchange in  $\text{La}_{1.7}\text{Ca}_{0.3}\text{Ni}_{1-y}\text{Cu}_y\text{O}_{4+\delta}$ , probably due to a decrease in oxygen excess from 0.05(1) to 0.00(1) (Table 3) and possible formation of oxygen vacancies in the perovskite layers at increased temperatures [86]. Conforming to [86], the rate of surface oxygen exchange in  $\text{La}_2\text{NiO}_{4+\delta}$  and  $\text{La}_{2-x}\text{Sr}_x\text{NiO}_{4+\delta}$  is limited by incorporation due to the limited availability of oxygen vacancies. The authors disregarded the direct incorporation of the adsorbed oxygen into the interstitial site and suggested that the charged ion first moves into an apical oxygen vacancy and only after that moves into the interstitial site. Within this concept, the formation of new vacancies at the surface of  $\text{La}_{1.7}\text{Ca}_{0.3}\text{Ni}_{1-y}\text{Cu}_y\text{O}_{4+\delta}$  with copper substitution, especially for highly doped samples, should promote surface exchange.

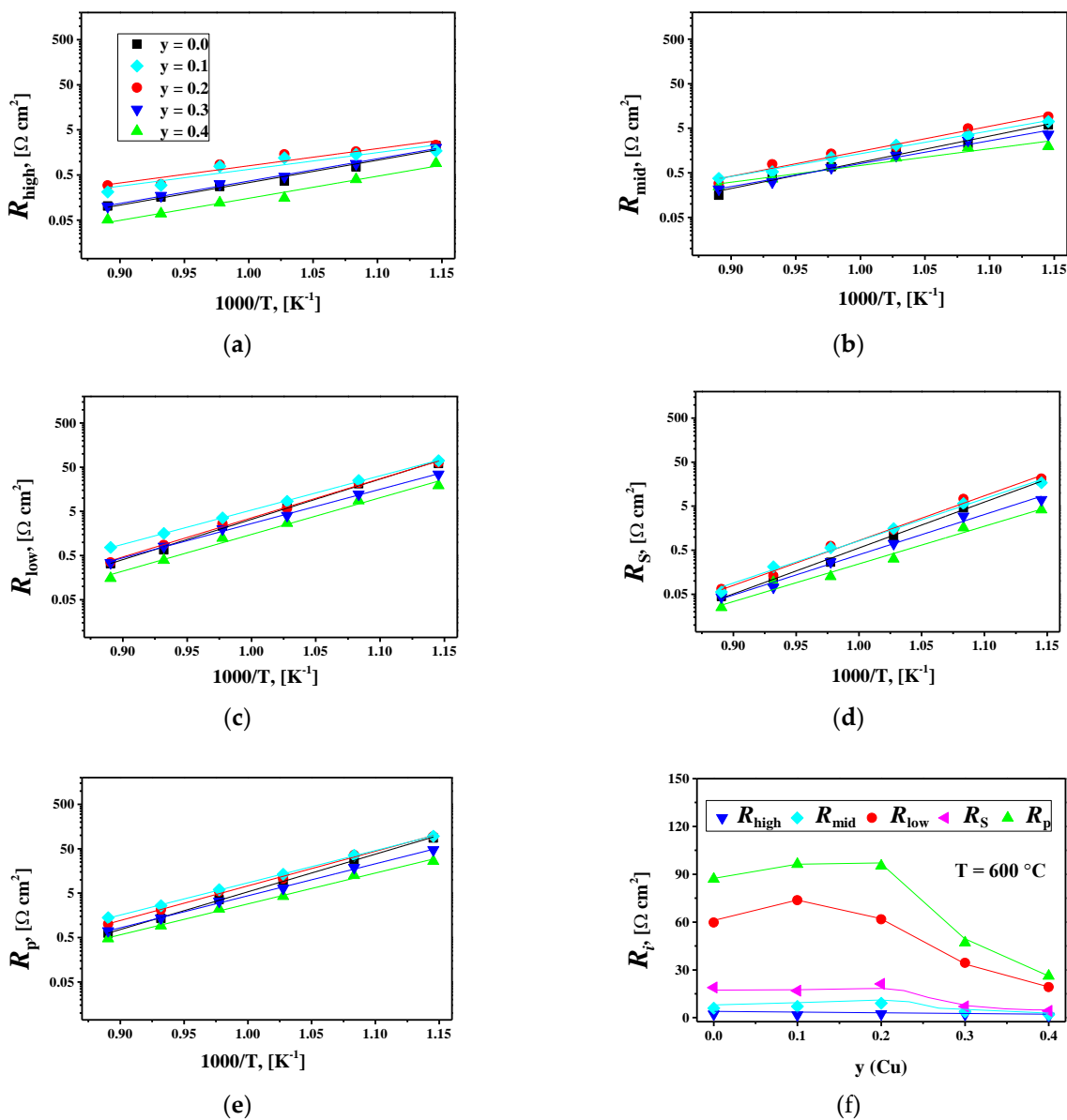


**Figure 9.** Partial contributions to the electrode polarization resistance and the total polarization resistance  $R_p$  on: (a–e) temperature, and (f) Cu content for the  $La_{1.7}Ca_{0.3}Ni_{1-y}Cu_yO_{4+\delta}/SDC$  symmetrical cells sintered at  $1000^\circ C$ .

In this way, the increase in the  $R_{low}$  values (and, consequently,  $R_p$ ) with copper doping in the range of  $0 \leq y \leq 0.2$  can be due to slower oxygen-ion transport due to decreasing the interstitial oxygen content, while the reduction in the  $R_{low}$  values at  $y > 0.2$  can be attributed to the facilitated surface exchange kinetics in these materials due to appearance of oxygen vacancies at the electrode operating temperatures. The microstructural factors and sinterability of the electrodes should also be taken into account. On the one hand, the electrodes with  $y = 0.3, 0.4$  present a more homogeneous microstructure compared to that for the oxides with  $0 \leq y \leq 0.2$ , while the gradual increase in grain size with copper doping of  $La_{1.7}Ca_{0.3}Ni_{1-y}Cu_yO_{4+\delta}$  indicates better sinterability and, consequently, better grain connectivity (Figure S4), which should improve the performance. On the other hand, the increased particle size (and the decreased specific surface area) at a higher copper content can deteriorate the electrode performance as is discussed further in the paper. The latter could be a more critical parameter since the reduction in sintering temperature significantly decreases the polarization resistance of  $La_{1.7}Ca_{0.3}Ni_{0.6}Cu_{0.4}O_{4+\delta}$

(see the next paragraph, Figure 10a and Figure S8). Hence, the microstructural factors should have a detrimental effect on the overall electrode performance. Still, the polarization resistance of  $\text{La}_{1.7}\text{Ca}_{0.3}\text{Ni}_{1-y}\text{Cu}_y\text{O}_{4+\delta}$  decreases when  $y > 0.2$  indicating that copper doping improves electrode performance despite the changes in microstructure, most probably, due to the enhanced surface oxygen exchange, as we discussed above. Nevertheless, more comprehensive research on the effect of the electrode microstructure on the polarization resistance, as well as studies on the bulk oxygen diffusion and surface oxygen exchange kinetics for  $\text{La}_{1.7}\text{Ca}_{0.3}\text{Ni}_{1-y}\text{Cu}_y\text{O}_{4+\delta}$  are necessary.

For further optimization of the  $\text{La}_{1.7}\text{Ca}_{0.3}\text{Ni}_{0.6}\text{Cu}_{0.4}\text{O}_{4+\delta}$ /SDC symmetrical cell, the effect of sintering temperature ( $T_S$ ) and the role of the  $\text{LaNi}_{0.6}\text{Fe}_{0.4}\text{O}_{3-\delta}$  (LNF) current collector were analyzed. The polarization resistance as a function of temperature for the  $\text{La}_{1.7}\text{Ca}_{0.3}\text{Ni}_{0.6}\text{Cu}_{0.4}\text{O}_{4+\delta}$ /SDC cells sintered at 900, 1000, and 1100 °C is shown in Figure 10a. One can see that the  $R_p$  values decrease when the sintering temperature is reduced from 1000 to 900 °C and significantly increase with the increase in  $T_S$  up to 1100 °C. This shows that  $T_S = 900$  °C is the optimal sintering temperature for the studied cells. The DFRTs calculated by the regularization method (as described above) and the resistances of separate contributions are shown in Figure 10b,c, respectively. The increase in  $T_S$  led to reduced  $R_{\text{high}}$  and  $R_{\text{mid}}$  resistances, i.e., it facilitated charge transfer processes.

Higher sintering temperatures should improve interfacial connectivity between the cell components promoting charge transfer. At the same time, the value of the low-frequency contribution  $R_S$  significantly increases with increasing  $T_S$ . This can be caused by the reduction in the specific surface area of the electrodes (an increase in the grain size), which leads to a decrease in the porosity of the electrode layers creating limitations for oxygen gas-phase diffusion toward the reaction sites. The reduced specific surface area could also limit the number of available sites for oxygen adsorption, slowing down the oxygen exchange process.

The reduction in the thickness of the LNF collector from 50 to 30 and then to 15  $\mu\text{m}$  in the cells sintered at 900 °C leads to a slight decrease in polarization resistance at  $T < 750$  °C, Figure 10a. Moreover, the  $\text{La}_{1.7}\text{Ca}_{0.3}\text{Ni}_{0.6}\text{Cu}_{0.4}\text{O}_{4+\delta}$ /SDC cell without the LNF collector shows the lowest polarization resistance, 1.95  $\Omega\text{cm}^2$  at 700 °C, compared to that of similar cells ( $T_S = 900$  °C) with the current collector layer. The analysis of separate contributions to the total polarization resistance, Figure 10d, shows that adding LNF as a collector increases the  $R_{\text{low}}$  and especially  $R_S$  values. Assuming that the  $R_S$  resistances are associated with oxygen gas-phase diffusion followed by surface exchange, one can conclude that the LNF layer hampers gas-phase oxygen transport to the electrode surface and induces limitations for surface exchange, thus increasing the  $R_{\text{low}}$  values.

It was shown earlier that the application of the LNF collector onto the copper-free  $\text{La}_{1.7}\text{Ca}_{0.3}\text{NiO}_{4+\delta}$  electrode led to a substantial decrease in the polarization resistance from 12.0 to 4.0  $\Omega\text{cm}^2$  at 700 °C (Table 1, Refs. [35,36]). However, one should note that the latter value is remarkably higher than  $R_p$  obtained for the single-layer  $\text{La}_{1.7}\text{Ca}_{0.3}\text{Ni}_{0.6}\text{Cu}_{0.4}\text{O}_{4+\delta}$  electrode in the present work under similar conditions. Thus, the copper substitution of  $\text{La}_{1.7}\text{Ca}_{0.3}\text{Ni}_{1-y}\text{Cu}_y\text{O}_{4+\delta}$  not only improves the overall electrochemical performance but also eliminates the need for an additional current collector layer. Summarizing, the increase in copper content in  $\text{La}_{1.7}\text{Ca}_{0.3}\text{Ni}_{1-y}\text{Cu}_y\text{O}_{4+\delta}$  up to  $y = 0.4$  reduces the optimal sintering temperature of electrodes of the SDC-based symmetric cells down to 900 °C and minimizes the polarization resistance down to 0.15, 0.31, 0.85 and 1.95  $\Omega\text{cm}^2$  at 850, 800, 750 and 700 °C, respectively.

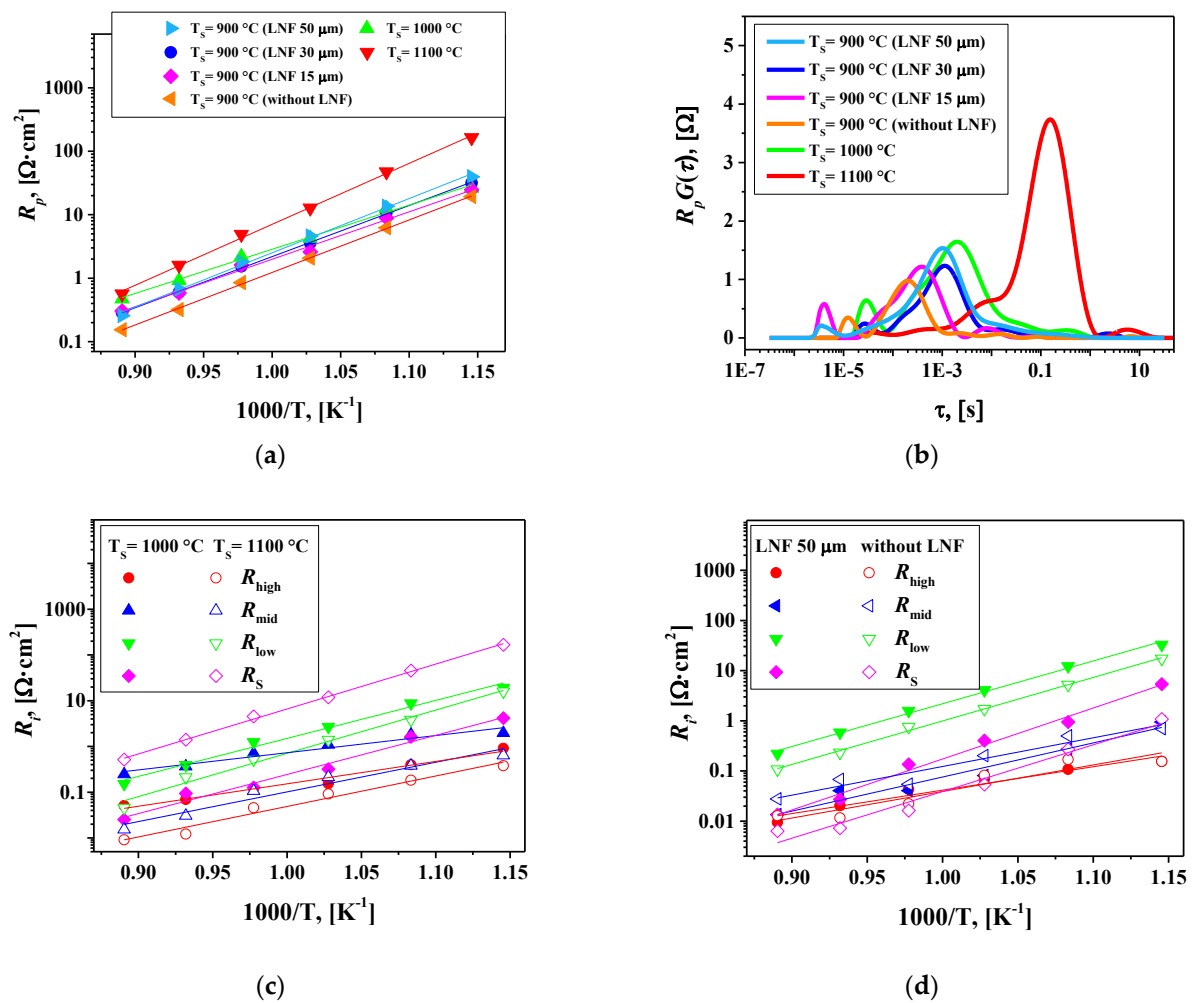


**Figure 10.** (a) Electrode polarization resistance versus temperature for different  $\text{La}_{1.7}\text{Ca}_{0.3}\text{Ni}_{0.6}\text{Cu}_{0.4}\text{O}_{4+\delta}/\text{SDC}$  cells; (b) DFRTs calculated by the regularization method at 800 °C; (c) partial contributions to  $R_p$  for the  $\text{La}_{1.7}\text{Ca}_{0.3}\text{Ni}_{0.6}\text{Cu}_{0.4}\text{O}_{4+\delta}/\text{SDC}$  cells fabricated at 1000 °C and 1100 °C; (d) partial contributions to  $R_p$  for the  $\text{La}_{1.7}\text{Ca}_{0.3}\text{Ni}_{0.6}\text{Cu}_{0.4}\text{O}_{4+\delta}/\text{SDC}$  cells fabricated at 900 °C with and without the LNF collector layer.

#### 4. Conclusions

In this study, the physicochemical properties and electrochemical performance of the  $\text{La}_{1.7}\text{Ca}_{0.3}\text{Ni}_{1-y}\text{Cu}_y\text{O}_{4+\delta}$  ( $y = 0.0\text{--}0.4$ ) nickelates as potential candidates for the application in the intermediate-temperature solid oxide fuel cells were investigated. The  $\text{La}_{1.7}\text{Ca}_{0.3}\text{Ni}_{1-y}\text{Cu}_y\text{O}_{4+\delta}$  ( $y = 0.0\text{--}0.4$ ) solid solutions synthesized via the conventional solid-state reaction method had a tetragonal structure (space group  $I4/mmm$ ). The unit cell parameter  $c$  and cell volume increased in the  $\text{La}_{1.7}\text{Ca}_{0.3}\text{Ni}_{1-y}\text{Cu}_y\text{O}_{4+\delta}$  series consistently with the larger size of Cu and with the concomitant decrease of the oxygen content in the lattice resulted in a moderate decrease in the total electrical conductivity value from  $103\text{ S cm}^{-1}$  ( $y = 0.0$ ) to  $91\text{ S cm}^{-1}$  ( $y = 0.4$ ) at 700 °C. The low concentration of the interstitial oxygen ions in the lattice as a result of the acceptor-type substitution with calcium resulted in a limited oxygen permeability of the Cu-substituted  $\text{La}_{1.7}\text{Ca}_{0.3}\text{Ni}_{0.6}\text{Cu}_{0.4}\text{O}_{4+\delta}$  membranes compared to the undoped lanthanum nickelate. Cu substitution was shown to have no visible influence on the oxygen permeability. Moreover, the high level of Cu substitution ( $y > 0.2$ ) allowed the reduction in the polarization resistance of the  $\text{La}_{1.7}\text{Ca}_{0.3}\text{Ni}_{1.6}\text{Cu}_{0.4}\text{O}_{4+\delta}$  electrodes in contact with  $\text{Ce}_{0.8}\text{Sm}_{0.2}\text{O}_{1.9}$  solid electrolyte from  $0.6\text{ }\Omega\text{ cm}^2$  ( $y = 0.0$ ) down to  $0.15\text{ }\Omega\text{ cm}^2$  ( $y = 0.4$ ) at 850 °C in air. This was accompanied by a decrease in the activation energy of the electrode process from 1.68 to 1.38 eV. The electrode performance enhance-

ment can be associated with facilitated surface exchange kinetics, as well as improvements in powder sintering and, accordingly, contact/adhesion both between the electrode and electrolyte and between grains.

The optimum sintering temperature of porous electrode layers was found to reduce from 1200 °C for  $y = 0.0$  to 900 °C for  $y = 0.4$ . In contrast to the copper-free  $\text{La}_{1.7}\text{Ca}_{0.3}\text{NiO}_{4+\delta}$  electrodes, the application of the  $\text{LaNi}_{0.6}\text{Fe}_{0.4}\text{O}_{3-\delta}$  collector layer on the  $\text{La}_{1.7}\text{Ca}_{0.3}\text{Ni}_{1.6}\text{Cu}_{0.4}\text{O}_{4+\delta}$  electrode had no positive impact on the electrochemical activity. The results of the present work imply that the designed single-layer  $\text{La}_{1.7}\text{Ca}_{0.3}\text{Ni}_{0.6}\text{Cu}_{0.4}\text{O}_{4+\delta}$  electrodes can be recommended for the application as cathodes in IT-SOFCs. The electrical properties and electrode performance can be further optimized using chemical techniques for the synthesis of fine  $\text{La}_{1.7}\text{Ca}_{0.3}\text{Ni}_{1-y}\text{Cu}_y\text{O}_{4+\delta}$  powders without ball milling and, consequently, excluding Si and Fe contaminations.

**Supplementary Materials:** The following supporting information can be downloaded at: <https://www.mdpi.com/article/10.3390/membranes12121222/s1>, Figure S1: SEM/EDS elemental distribution maps of the  $\text{La}_{1.7}\text{Ca}_{0.3}\text{NiO}_{4+\delta}$  powder; Figure S2: SEM/EDS elemental distribution maps of the  $\text{La}_{1.7}\text{Ca}_{0.3}\text{Ni}_{0.8}\text{Cu}_{0.2}\text{O}_{4+\delta}$  powder; Figure S3: SEM/EDS elemental distribution maps of the  $\text{La}_{1.7}\text{Ca}_{0.3}\text{Ni}_{0.6}\text{Cu}_{0.4}\text{O}_{4+\delta}$  powder; Figure S4: Crystal structure of  $\text{La}_{1.7}\text{Ca}_{0.3}\text{Ni}_{1-y}\text{Cu}_y\text{O}_{4+\delta}$ ; Figure S5: Concentration dependencies of the total conductivity of the  $\text{La}_{1.7}\text{Ca}_{0.3}\text{Ni}_{1-y}\text{Cu}_y\text{O}_{4+\delta}$  compact samples collected in air; Figure S6: SEM/EDS: fractured surface of  $\text{La}_{1.7}\text{Ca}_{0.3}\text{Ni}_{0.8}\text{Cu}_{0.2}\text{O}_{4+\delta}$  ceramics sintered at 1380 °C; Figure S7: Particles size distribution in the  $\text{La}_{1.7}\text{Ca}_{0.3}\text{Ni}_{1-y}\text{Cu}_y\text{O}_{4+\delta}$  electrodes based on the SEM data; Figure S8: SEM/EDS elemental distribution maps of the  $\text{La}_{1.7}\text{Ca}_{0.3}\text{NiO}_{4+\delta}$  electrode surface ( $T_S = 1000$  °C); Figure S9: SEM/EDS elemental distribution maps of the  $\text{La}_{1.7}\text{Ca}_{0.3}\text{Ni}_{0.8}\text{Cu}_{0.2}\text{O}_{4+\delta}$  electrode surface ( $T_S = 1000$  °C); Figure S10: SEM/EDS elemental distribution maps of the  $\text{La}_{1.7}\text{Ca}_{0.3}\text{Ni}_{0.6}\text{Cu}_{0.4}\text{O}_{4+\delta}$  electrode surface ( $T_S = 1000$  °C); Figure S11: Influence of electrode sintering temperature on the polarization resistance of  $\text{La}_{1.7}\text{Ca}_{0.3}\text{Ni}_{1-y}\text{Cu}_y\text{O}_{4+\delta}$  electrodes in contact with SDC solid electrolyte; Table S1: Impurity content and specific surface area of the  $\text{La}_{1.7}\text{Ca}_{0.3}\text{Ni}_{1-y}\text{Cu}_y\text{O}_{4+\delta}$  powders after the two-stage synthesis with intermediate and final milling; Table S2: Impurity content in the  $\text{La}_{1.7}\text{Ca}_{0.3}\text{Ni}_{1-y}\text{Cu}_y\text{O}_{4+\delta}$  powders determined by SEM/EDS analysis; Table S3: Chemical composition of  $\text{La}_{1.7}\text{Ca}_{0.3}\text{Ni}_{1-y}\text{Cu}_y\text{O}_{4+\delta}$  electrodes determined by SEM/EDS analysis of the electrode surface.

**Author Contributions:** Conceptualization, E.F. and E.P.; validation, E.F., A.Y. and E.P.; formal analysis, E.F. and A.G.; investigation, N.P., T.M., K.Z. and S.P.; resources, E.P.; data curation, A.G.; writing—original draft preparation, E.F. and A.G.; writing—review and editing, A.Y. and E.P.; visualization, E.F., N.P. and A.G.; supervision, A.Y.; project administration, E.P. and E.F.; funding acquisition, E.P. and A.Y. All authors have read and agreed to the published version of the manuscript.

**Funding:** K.Z. and A.Y. gratefully acknowledge financial support by the project CARBOSTEAM (POCI-01-0145-FEDER-032295) funded by FEDER through COMPETE2020–Programa Operacional Competitividade e Internacionalização (POCI) and by national funds through FCT/MCTES, and by project CICECO–Aveiro Institute of Materials (UIDB/50011/2020, UIDP/50011/2020 & LA/P/0006/2020) financed by national funds through the FCT/MCTES (PIDDAC). K.Z. acknowledges PhD scholarship by the FCT (SFRH/BD/138773/2018). E.P. is grateful to the research funding from the Ministry of Science and Higher Education of the Russian Federation (Ural Federal University Program of Development within the Priority-2030 Program).

**Institutional Review Board Statement:** Not applicable.

**Informed Consent Statement:** Not applicable.

**Data Availability Statement:** Not applicable.

**Acknowledgments:** The electrode fabrication and study of the electrochemical performance was performed in the framework of the government task IHTE UB RAS number 122020100324-3 and T.M. PhD scholarship. The authors thank Dmitry Malyskin for the help with SEM investigations, Alexander Kolchugin and Alexander Dmitriev for valuable comments. The work was partly done using the equipment of the collective centers Composition of Compounds (IHTE UB RAS) and Ural-M (IMET UB RAS).

**Conflicts of Interest:** The authors declare no conflict of interest.

## References

1. Singla, M.K.; Nijhawan, P.; Oberoi, A.S. Hydrogen fuel and fuel cell technology for cleaner future: A review. *Environ. Sci. Pollut. Res.* **2021**, *28*, 15607–15626. [[CrossRef](#)] [[PubMed](#)]
2. Sazali, N. Emerging technologies by hydrogen: A review. *Int. J. Hydrogen Energy* **2020**, *45*, 18753–18771. [[CrossRef](#)]
3. Zeng, S.; Yan, Z.; Yang, J. Review and forecast of ground heat exchangers development: A bibliometric analysis from 2001 to 2020. *Sustain. Energy Technol. Assess.* **2021**, *47*, 101547. [[CrossRef](#)]
4. Aqachmar, Z.; Ben Sassi, H.; Lahrech, K.; Barhdadi, A. Solar technologies for electricity production: An updated review. *Int. J. Hydrogen Energy* **2021**, *46*, 30790–30817. [[CrossRef](#)]
5. Azam, A.; Ahmed, A.; Wang, H.; Wang, Y.; Zhang, Z. Knowledge structure and research progress in wind power generation (WPG) from 2005 to 2020 using CiteSpace based scientometric analysis. *J. Clean. Prod.* **2021**, *295*, 126496. [[CrossRef](#)]
6. Surti, P.; Kailasa, S.K.; Mungray, A.K. Genetic engineering strategies for performance enhancement of bioelectrochemical systems: A review. *Sustain. Energy Technol. Assess.* **2021**, *47*, 101332. [[CrossRef](#)]
7. Santoro, C.; Garcia, M.J.S.; Walter, X.A.; You, J.; Theodosiou, P.; Gajda, I.; Obata, O.; Winfield, J.; Greenman, J.; Ieropoulos, I. Urine in bioelectrochemical systems: An overall review. *ChemElectroChem* **2020**, *7*, 1312–1331. [[CrossRef](#)]
8. Baykara, S.Z. Hydrogen: A brief overview on its sources, production and environmental impact. *Int. J. Hydrogen Energy* **2018**, *43*, 10605–10614. [[CrossRef](#)]
9. Singh, M.; Zappa, D.; Comini, E. Solid oxide fuel cell: Decade of progress, future perspectives and challenges. *Int. J. Hydrogen Energy* **2021**, *46*, 27643–27674. [[CrossRef](#)]
10. Abdalla, A.M.; Hossain, S.; Petra, P.M.; Ghasemi, M.; Azad, A.K. Achievements and trends of solid oxide fuel cells in clean energy field: A perspective review. *Front. Energy* **2020**, *14*, 359–382. [[CrossRef](#)]
11. Yang, B.; Guo, Z.; Wang, J.; Wang, J.; Zhu, T.; Shu, H.; Qiu, G.; Chen, J.; Zhang, J. Solid oxide fuel cell systems fault diagnosis: Critical summarization, classification, and perspectives. *J. Energy Storage* **2021**, *34*, 102153. [[CrossRef](#)]
12. Zhu, P.; Yao, J.; Qian, C.; Yang, F.; Porpatham, E.; Zhang, Z.; Wu, Z. High-efficiency conversion of natural gas fuel to power by an integrated system of SOFC, HCCI engine, and waste heat recovery: Thermodynamic and thermo-economic analyses. *Fuel* **2020**, *275*, 117883. [[CrossRef](#)]
13. Zhang, X.; Jin, Y.; Li, D.; Xiong, Y. A review on recent advances in micro-tubular solid oxide fuel cells. *J. Power Sources* **2021**, *506*, 230135. [[CrossRef](#)]
14. Su, H.; Hu, Y.H. Progress in low-temperature solid oxide fuel cells with hydrocarbon fuels. *J. Chem. Eng.* **2020**, *402*, 126235. [[CrossRef](#)]
15. Radenahmad, N.; Azad, A.T.; Saghir, M.; Taweekun, J.; Bakar, M.S.A.; Reza, M.S.; Azad, A.K. A review on biomass derived syngas for SOFC based combined heat and power application. *Renew. Sustain. Energy Rev.* **2020**, *119*, 109560. [[CrossRef](#)]
16. Saadabadi, S.A.; ThallamThattai, A.; Fan, L.; Lindeboom, R.E.F.; Spanjers, H.; Aravind, P.V. Solid oxide fuel cells fuelled with biogas: Potential and constraints. *Renew. Energy* **2019**, *134*, 194–214. [[CrossRef](#)]
17. Sreedhar, I.; Agarwal, B.; Goyal, P.; Agarwal, A. An overview of degradation in solid oxide fuel cells-potential clean power sources. *J. Solid State Electrochem.* **2020**, *24*, 1239–1270. [[CrossRef](#)]
18. Horita, T. Chromium poisoning for prolonged lifetime of electrodes in solid oxide fuel cells—review. *Ceram. Intern.* **2021**, *47*, 7293–7306. [[CrossRef](#)]
19. Zhang, L.; Chen, G.; Dai, R.; Lv, X.; Yang, D.; Geng, S. A review of the chemical compatibility between oxide electrodes and electrolytes in solid oxide fuel cells. *J. Power Sources* **2021**, *492*, 229630. [[CrossRef](#)]
20. Bello, I.T.; Zhai, S.; He, Q.; Xu, Q.; Ni, M. Scientometric review of advancements in the development of high-performance cathode for low and intermediate temperature solid oxide fuel cells: Three decades in retrospect. *Int. J. Hydrogen Energy* **2021**, *46*, 26518–26536. [[CrossRef](#)]
21. Richter, J.; Holtappels, P.; Graule, T.; Nakamura, T.; Gauckler, L.J. Materials design for perovskite SOFC cathodes. *Monatsh. Chem.* **2009**, *140*, 985–999. [[CrossRef](#)]
22. Ding, P.; Li, W.; Zhao, H.; Wu, C.; Zhao, L.; Dong, B.; Wang, S. Review on Ruddlesden–Popper perovskites as cathode for solid oxide fuel cells. *J. Phys. Mater.* **2021**, *4*, 022002. [[CrossRef](#)]
23. Sadykov, V.A.; Sadovskaya, E.M.; Ereemeev, N.F.; Yu Pikalova, E.; Bogdanovich, N.M.; Filonova, E.A.; Krieger, T.A.; Fedorova, Y.E.; Krasnov, A.V.; Skriabin, P.I.; et al. Novel materials for solid oxide fuel cells cathodes and oxygen separation membranes: Fundamentals of oxygen transport and performance. *Carbon Resour. Convers.* **2020**, *3*, 112–121. [[CrossRef](#)]
24. Tarutin, A.P.; Lyagaeva, J.G.; Medvedev, D.A.; Bi, L.; Yaremchenko, A.A. Recent advances in layered  $\text{Ln}_2\text{NiO}_{4+\delta}$  nickelates: Fundamentals and prospects of their applications in protonic ceramic fuel and electrolysis cells. *J. Mater. Chem. A* **2021**, *9*, 154–195. [[CrossRef](#)]
25. Wu, C.H.; Shi, Y.J.; Lu, F.; Jia, X.S.; Su, J.R.; He, H.; Cai, B. Ruddlesden–Popper-type  $\text{La}_{1.5-x}\text{Eu}_x\text{Pr}_{0.5}\text{Ni}_{0.9}\text{Cu}_{0.1}\text{O}_{4+\delta}$  as a potential cathode material for H-SOFCs. *Phys. Solid State* **2021**, *63*, 775–784. [[CrossRef](#)]
26. Ma, J.; Pan, Y.; Wang, Y.; Chen, Y. A Sr and Ni doped Ruddlesden–Popper perovskite oxide  $\text{La}_{1.6}\text{Sr}_{0.4}\text{Cu}_{0.6}\text{Ni}_{0.4}\text{O}_{4+\delta}$  as a promising cathode for protonic ceramic fuel cells. *J. Power Sources* **2021**, *509*, 230369. [[CrossRef](#)]
27. Wang, W.; Li, Y.; Liu, Y.; Tian, Y.; Ma, B.; Li, J.; Pu, J.; Chi, B. Ruddlesden–Popper-structured  $(\text{Pr}_{0.9}\text{La}_{0.1})_2(\text{Ni}_{0.8}\text{Cu}_{0.2})\text{O}_{4+\delta}$ : An effective oxygen electrode material for proton-conducting solid oxide electrolysis cells. *ACS Sustain. Chem. Eng.* **2021**, *9*, 10913–10919. [[CrossRef](#)]

28. Geffroy, P.-M.; Reichmann, M.; Chartier, T.; Bassat, J.-M.; Grenier, J.-C. Evaluating oxygen diffusion, surface exchange and oxygen semi-permeation in  $\text{Ln}_2\text{NiO}_{4+\delta}$  membranes (Ln=La, Pr and Nd). *J. Membr. Sci.* **2014**, *451*, 234–242. [[CrossRef](#)]
29. Flura, A.; Dru, S.; Nicollet, C.; Vibhu, V.; Fourcade, S.; Lebraud, E.; Rougier, A.; Bassat, J.-M.; Grenier, J.-C. Chemical and structural changes in  $\text{Ln}_2\text{NiO}_4$  (Ln=La, Pr or Nd) lanthanide nickelates as a function of oxygen partial pressure at high temperature. *J. Solid State Chem.* **2015**, *228*, 189–198. [[CrossRef](#)]
30. Aguadero, A.; Escudero, M.J.; Pérez, M.; Alonso, J.A.; Pomjakushin, V.; Daza, L. Effect of Sr content on the crystal structure and electrical properties of the system  $\text{La}_{2-x}\text{Sr}_x\text{NiO}_{4+\delta}$  ( $0 \leq x \leq 1$ ). *Dalton Trans.* **2006**, *36*, 4377–4383. [[CrossRef](#)]
31. Sadykov, V.A.; Sadovskaya, E.M.; Pikalova, E.Y.; Kolchugin, A.A.; Filonova, E.A.; Pikalov, S.M.; Ereemeev, N.F.; Ishchenko, A.V.; Lukashevich, A.I.; Bassat, J.M. Transport features in layered nickelates: Correlation between structure, oxygen diffusion, electrical and electrochemical properties. *Ionics* **2018**, *24*, 1181–1193. [[CrossRef](#)]
32. Tarutin, A.P.; Lyagaeva, J.G.; Farlenkov, A.S.; Vylkov, A.I.; Medvedev, D.M. Cu-Substituted  $\text{La}_2\text{NiO}_{4+\delta}$  as oxygen electrodes for protonic ceramic electrochemical cells. *Ceram. Intern.* **2019**, *45*, 16105–16112. [[CrossRef](#)]
33. Aguadero, A.; Alonso, J.; Escudero, M.; Daza, L. Evaluation of the  $\text{La}_2\text{Ni}_{1-x}\text{Cu}_x\text{O}_{4+\delta}$  system as SOFC cathode material with 8YSZ and LSGM as electrolytes. *Solid State Ionics* **2008**, *179*, 393–400. [[CrossRef](#)]
34. Pikalova, E.Y.; Bogdanovich, N.M.; Kolchugin, A.A.; Osinkin, D.A.; Bronin, D.I. Electrical and electrochemical properties of  $\text{La}_2\text{NiO}_{4+\delta}$ -based cathodes in contact with  $\text{Ce}_{0.8}\text{Sm}_{0.2}\text{O}_{2-\delta}$  electrolyte. *Procedia Eng.* **2014**, *98*, 105–110. [[CrossRef](#)]
35. Kolchugin, A.A.; Pikalova, E.Y.; Bogdanovich, N.M.; Bronin, D.I.; Filonova, E.A. Electrochemical properties of doped lanthanum-nickelate-based electrodes. *Russ. J. Electrochem.* **2017**, *53*, 826–833. [[CrossRef](#)]
36. Pikalova, E.Y.; Kolchugin, A.A.; Sadykov, V.A.; Sadovskaya, E.M.; Filonova, E.A.; Ereemeev, N.F.; Bogdanovich, N.M. Structure, transport properties and electrochemical behavior of the layered lanthanide nickelates doped with calcium. *Int. J. Hydrogen Energy* **2018**, *43*, 17373–17386. [[CrossRef](#)]
37. Shen, Y.; Zhao, H.; Świerczek, K.; Du, Z.; Xie, Z. Lattice structure, sintering behavior and electrochemical performance of  $\text{La}_{1.7}\text{Ca}_{0.3}\text{Ni}_{1-x}\text{Cu}_x\text{O}_{4+\delta}$  as cathode material for intermediate-temperature solid oxide fuel cell. *J. Power Sources* **2013**, *240*, 759–765. [[CrossRef](#)]
38. Wu, X.; Gu, C.; Cao, J.; Miao, L.; Fu, C.; Liu, W. Investigations on electrochemical performance of  $\text{La}_2\text{NiO}_{4+\delta}$  cathode material doped at A site for solid oxide fuel cells. *Mater. Res. Express* **2020**, *7*, 065507. [[CrossRef](#)]
39. Kravchenko, E.; Zakharchuk, K.; Viskup, A.; Grins, J.; Svensson, G.; Pankov, V.; Yaremchenko, A. Impact of oxygen deficiency on the electrochemical performance of  $\text{K}_2\text{NiF}_4$ -type  $(\text{La}_{1-x}\text{Sr}_x)_2\text{NiO}_{4-\delta}$  oxygen electrodes. *ChemSusChem* **2017**, *10*, 600–611. [[CrossRef](#)]
40. Lyagaeva, Y.G.; Danilov, N.A.; Gorshkov, M.Y.; Vdovin, G.K.; Antonov, B.D.; Demin, A.K.; Medvedev, D.A. Functionality of lanthanum, neodymium, and praseodymium nickelates as promising electrode systems for proton-conducting electrolytes. *Russ. J. Appl. Chem.* **2018**, *91*, 583–590. [[CrossRef](#)]
41. Sadykov, V.A.; Pikalova, E.Y.; Kolchugin, A.A.; Fetisov, A.V.; Sadovskaya, E.M.; Filonova, E.A.; Ereemeev, N.F.; Goncharov, V.B.; Krasnov, A.V.; Skriabin, P.I.; et al. Transport properties of Ca-doped  $\text{Ln}_2\text{NiO}_4$  for intermediate temperature solid oxide fuel cells cathodes and catalytic membranes for hydrogen production. *Int. J. Hydrogen Energy* **2020**, *45*, 13625–13642. [[CrossRef](#)]
42. Pikalova, E.; Sadykov, V.; Sadovskaya, E.; Yeremeev, N.; Kolchugin, A.; Shmakov, A.; Vinokurov, Z.; Mishchenko, D.; Filonova, E.; Belyaev, V. Correlation between structural and transport properties of Ca-doped La nickelates and their electrochemical performance. *Crystals* **2021**, *11*, 297. [[CrossRef](#)]
43. Myung, J.; Shin, T.H.; Huang, X.; Savaniu, C.; Irvine, J.  $\text{La}_{1.7}\text{Ca}_{0.3}\text{Ni}_{0.75}\text{Cu}_{0.25}\text{O}_{4-\delta}$ -layered perovskite as cathode on  $\text{La}_{0.9}\text{Sr}_{0.1}\text{Ga}_{0.8}\text{Mg}_{0.2}\text{O}_3$  or  $\text{Ce}_{0.8}\text{Gd}_{0.2}\text{O}_2$  electrolyte for intermediate temperature solid oxide fuel cells. *Int. J. Appl. Ceram. Technol.* **2016**, *13*, 269–273. [[CrossRef](#)]
44. Tsipis, E.V.; Kharton, V.V.; Frade, J.R. Electrochemical behavior of mixed-conducting oxide cathodes in contact with apatite-type  $\text{La}_{10}\text{Si}_5\text{AlO}_{26.5}$  electrolyte. *Electrochim. Acta* **2007**, *52*, 4428–4435. [[CrossRef](#)]
45. Huang, X.; Shin, T.H.; Zhou, J.; Irvine, J.T.S. Hierarchically nanoporous  $\text{La}_{1.7}\text{Ca}_{0.3}\text{CuO}_{4-\delta}$  and  $\text{La}_{1.7}\text{Ca}_{0.3}\text{Ni}_x\text{Cu}_{1-x}\text{O}_{4-\delta}$  ( $0.25 \leq x \leq 0.75$ ) as potential cathode materials for IT-SOFCs. *J. Mater. Chem. A* **2015**, *3*, 13468–13475. [[CrossRef](#)]
46. Gilev, A.R.; Kiselev, E.A.; Zakharov, D.M.; Cherepanov, V.A. Effect of calcium and copper/iron co-doping on defect-induced properties of  $\text{La}_2\text{NiO}_4$ -based materials. *J. Alloys Compd.* **2018**, *753*, 491–501. [[CrossRef](#)]
47. FullProf Suite. Crystallographic Tools for Rietveld, Profile Matching and Integrated-Intensity Refinements of X-ray and/or Neutron Data. Available online: <https://www.ill.eu/sites/fullprof/> (accessed on 11 October 2022).
48. Kovalevsky, A.V.; Yaremchenko, A.A.; Kolotygin, V.A.; Shaula, A.L.; Kharton, V.V.; Snijkers, F.M.M.; Buekenhoudt, A.; Frade, J.R.; Naumovich, E.N. Processing and oxygen permeation studies of asymmetric multilayer  $\text{Ba}_{0.5}\text{Sr}_{0.5}\text{Co}_{0.8}\text{Fe}_{0.2}\text{O}_{3-\delta}$  membranes. *J. Membr. Sci.* **2011**, *380*, 68–80. [[CrossRef](#)]
49. Pikalova, E.Y.; Bogdanovich, N.M.; Kolchugin, A.A.; Ananyev, M.V.; Pankratov, A.A. Influence of the synthesis method on the electrochemical properties of bilayer electrodes based on  $\text{La}_2\text{NiO}_{4+\delta}$  and  $\text{LaNi}_{0.6}\text{Fe}_{0.4}\text{O}_{3-\delta}$ . *Solid State Ion.* **2016**, *288*, 36–42. [[CrossRef](#)]
50. Osinkin, D.; Gavriluk, A.L.; Bronin, D.I. The Use of Tikhonov Regularization Method for calculating the Distribution Function of Relaxation Times in impedance spectroscopy. *Russ. J. Electrochem.* **2017**, *53*, 575–588. [[CrossRef](#)]
51. Wan, T.H.; Saccoccio, M.; Chen, C.; Ciucci, F. Influence of the Discretization Methods on the Distribution of Relaxation Times Deconvolution: Implementing Radial Basis Functions with DRT tools. *Electrochim. Acta* **2015**, *184*, 483–499. [[CrossRef](#)]

52. Ganguly, P.; Rao, C.N.R. Crystal chemistry and magnetic properties of layered metal oxides possessing the  $K_2NiF_4$  or related structures. *J. Solid State Chem.* **1984**, *53*, 193–216. [[CrossRef](#)]
53. Choisnet, J. Structure and bonding anisotropy in intergrowth oxides: A clue to the manifestation of bidimensionality in T-, T'-, and T\*-type structures. *J. Solid State Chem.* **1999**, *147*, 379–389. [[CrossRef](#)]
54. Shannon, R.D. Revised effective ionic radii and systematic Studies of interatomic distances in halides and chalcogenides. *Acta Cryst. A* **1976**, *32*, 751–767. [[CrossRef](#)]
55. Wang, C.; Soga, H.; Okiba, T.; Niwa, E.; Hashimoto, T. Construction of structural phase diagram of  $Nd_2Ni_{1-x}Cu_xO_{4+\delta}$  and effect of crystal structure and phase transition on electrical conduction behavior. *Mat. Res. Bull.* **2019**, *111*, 61–69. [[CrossRef](#)]
56. Khandale, A.P.; Bansod, M.G.; Bhoga, S.S. Improved electrical and electrochemical performance of co-doped  $Nd_{1.8}Sr_{0.2}Ni_{1-x}Cu_xO_{4+\delta}$ . *Solid State Ion.* **2015**, *276*, 127–135. [[CrossRef](#)]
57. Filonova, E.A.; Pikalova, E.Y.; Maksimchuk, T.Y.; Vylkov, A.I.; Pikalov, S.M.; Maignan, A. Crystal structure and functional properties of  $Nd_{1.6}Ca_{0.4}Ni_{1-y}Cu_yO_{4+\delta}$  as prospective cathode materials for intermediate temperature solid oxide fuel cells. *Int. J. Hydrogen Energy* **2021**, *46*, 17037–17050. [[CrossRef](#)]
58. Bansod, M.B.; Khandale, A.P.; Kumar, R.V.; Bhoga, S.S. Crystal structure, electrical and electrochemical properties of Cu co-doped  $Pr_{1.3}Sr_{0.7}NiO_{4+\delta}$  mixed ionic-electronic conductors (MIECs). *Int. J. Hydrogen Energy* **2018**, *43*, 373–384. [[CrossRef](#)]
59. Sakai, M.; Wang, C.; Okiba, T.; Soga, H.; Niwa, E.; Hashimoto, T. Thermal analysis of structural phase transition behavior of  $Ln_2Ni_{1-x}Cu_xO_{4+\delta}$  (Ln = Nd, Pr) under various oxygen partial pressures. *J. Therm. Anal. Calorim.* **2019**, *135*, 2765–2774. [[CrossRef](#)]
60. Kanai, H.; Mizusaki, J.; Tagawa, H.; Hoshiyama, S.; Hirano, K.; Fujita, K.; Tezuka, M.; Hashimoto, T. Defect chemistry of  $La_{2-x}Sr_xCuO_{4-\delta}$ : Oxygen nonstoichiometry and thermodynamic stability. *J. Solid State Chem.* **1997**, *131*, 150–159. [[CrossRef](#)]
61. Naumovich, E.N.; Patrakeev, M.V.; Kharton, V.V.; Yaremchenko, A.A.; Logvinovich, D.I.; Marques, F.M.B. Oxygen nonstoichiometry in (M = Cu, Co) under oxidizing conditions. *Solid State Sci.* **2005**, *7*, 1353–1362. [[CrossRef](#)]
62. Boehm, E.; Bassat, J.-M.; Steil, M.C.; Dordor, P.; Mauvy, F.; Grenier, J.-C. Oxygen transport properties of  $La_2Ni_{1-x}Cu_xO_{4+\delta}$  mixed conducting oxides. *Solid State Sci.* **2003**, *5*, 973–981. [[CrossRef](#)]
63. Zhao, C.; Zhou, Q.; Zhang, T.; Qu, L.; Yang, X.; Wei, T. Preparation and electrochemical properties of  $La_{1.5}Pr_{0.5}NiO_4$  and  $La_{1.5}Pr_{0.5}Ni_{0.9}Cu_{0.1}O_4$  cathode materials for intermediate-temperature solid oxide fuel cells. *Mat. Res. Bull.* **2019**, *113*, 25–30. [[CrossRef](#)]
64. Zhang, T.; Zhou, Q.; He, Y.; Zhao, C.; Qi, S.; Wang, M.; Wei, T.; An, D. Assessment of  $Nd_{1.5}Pr_{0.5}Ni_{1-x}M_xO_{4+\delta}$  (M = Cu, Co, Mo; x = 0, 0.05 and 0.1) as cathode materials for intermediate-temperature solid oxide fuel cell. *J. Mater. Sci. Mater. Electron.* **2020**, *31*, 949–958. [[CrossRef](#)]
65. Zakharchuk, K.; Bamburov, A.; Naumovich, E.N.; Vieira, M.A.; Yaremchenko, A.A. Impact of silica additions on the phase composition and electrical transport properties of Ruddlesden-Popper  $La_2NiO_{4+\delta}$  mixed conducting ceramics. *Processes* **2022**, *10*, 82. [[CrossRef](#)]
66. Tsvinkinberg, V.A.; Tolkacheva, A.S.; Filonova, E.A.; Gyrdasova, O.I.; Pikalov, S.M.; Vorotnikov, V.A.; Vylkov, A.I.; Moskalenko, N.I.; Pikalova, E.Y. Structure, thermal expansion and electrical conductivity of  $La_{2-x}Gd_xNiO_{4+\delta}$  ( $0.0 \leq x \leq 0.6$ ) cathode materials for SOFC applications. *J. Alloys Compd.* **2021**, *853*, 156728. [[CrossRef](#)]
67. Pikalova, E.; Kolchugin, A.; Zakharchuk, K.; Boiba, D.; Tsvinkinberg, V.; Filonova, E.; Khrustov, A.; Yaremchenko, A. Mixed ionic-electronic conductivity, phase stability and electrochemical activity of Gd-substituted  $La_2NiO_{4+\delta}$  as oxygen electrode material for solid oxide fuel/electrolysis cells. *Int. J. Hydrogen Energy* **2021**, *46*, 16932–16946. [[CrossRef](#)]
68. Filonova, E.A.; Russkikh, O.V.; Skutina, L.S.; Vylkov, A.I.; Maksimchuk, T.Y.; Ostroushko, A.A.  $Sr_2Ni_{0.7}Mg_{0.3}MoO_{6-\delta}$ : Correlation between synthesis conditions and functional properties as anode material for intermediate-temperature SOFCs. *Int. J. Hydrogen Energy* **2021**, *46*, 35910–35922. [[CrossRef](#)]
69. Martinson, K.D.; Belyak, V.E.; Sakhno, D.D.; Kiryanov, N.V.; Chebanenko, M.I.; Popkov, V.I. Effect of fuel type on solution combustion synthesis and photocatalytic activity of  $NiFe_2O_4$  nanopowders. *Nanosystems: Phys. Chem. Math.* **2021**, *12*, 792–798. [[CrossRef](#)]
70. Smirnova, M.N.; Kop'eva, M.A.; Beresnev, E.N.; Goeva, L.V.; Simonenko, N.P.; Nikiforova, G.E.; Ketsko, V.A. Synthesis of  $MgFe_{1.6}Ga_{0.4}O_4$  by gel combustion using glycine and hexamethylenetetramine. *Russ. J. Inorg. Chem.* **2018**, *63*, 439–443. [[CrossRef](#)]
71. Khaliullin, S.M.; Koshkina, A.A. Influence of fuel on phase formation, morphology, electric and dielectric properties of iron oxides obtained by SCS method. *Ceram. Int.* **2021**, *47*, 11942–11950. [[CrossRef](#)]
72. Baseri, J.; Naghizadeh, R.; Rezaie, H.R.; Golestanifard, F.; Golmohammad, M. A Comparative study on citrate sol-gel and combustion synthesis methods of  $CoAl_2O_4$  spinel. *Int. J. Appl. Ceram. Technol.* **2020**, *17*, 2709–2715. [[CrossRef](#)]
73. Nakamura, T.; Yashiro, K.; Sato, K.; Mizusaki, J. Oxygen nonstoichiometry and defect equilibrium in  $La_{2-x}Sr_xNiO_{4+\delta}$ . *Solid State Ion.* **2009**, *180*, 368–376. [[CrossRef](#)]
74. Tropin, E.S.; Ananyev, M.V.; Farlenkov, A.S.; Khodimchuk, A.V.; Berenov, A.V.; Fetisov, A.V.; Eremin, V.A.; Kolchugin, A.A. Surface defect chemistry and oxygen exchange kinetics in  $La_{2-x}Ca_xNiO_{4+\delta}$ . *J. Solid State Chem.* **2018**, *262*, 199–213. [[CrossRef](#)]
75. Kolchugin, A.A.; Pikalova, E.Y.; Bogdanovich, N.M.; Bronin, D.I.; Pikalov, S.M.; Plaksin, S.V.; Ananyev, M.V.; Eremin, V.A. Structural, electrical and electrochemical properties of calcium-doped lanthanum nickelate. *Solid State Ion.* **2016**, *288*, 48–53. [[CrossRef](#)]
76. Kharton, V.V.; Kovalevsky, A.V.; Avdeev, M.; Tsipis, E.V.; Patrakeev, M.V.; Yaremchenko, A.A.; Naumovich, E.N.; Frade, J.R. Chemically induced expansion of  $La_2NiO_{4+\delta}$ -based materials. *Chem. Mater.* **2007**, *19*, 2027–2033. [[CrossRef](#)]

77. Pikalova, E.Y.; Maragou, V.I.; Demina, A.N.; Demin, A.K.; Tsiakaras, P.E. The effect of co-dopant addition on the properties of  $\text{Ln}_{0.2}\text{Ce}_{0.8}\text{O}_{2-\delta}$  (Ln=Gd, Sm, La) solid-state electrolyte. *J. Power Sources* **2008**, *181*, 199–206. [[CrossRef](#)]
78. Boukamp, B.A.; Rolle, A. Analysis and application of Distribution of Relaxation Times in solid state ionic. *Solid State Ion.* **2017**, *302*, 12–18. [[CrossRef](#)]
79. Dion, F.; Lasia, A. The use of Regularization Methods in the Deconvolution of Underlying Distributions in electrochemical processes. *J. Electroanal. Chem.* **1999**, *475*, 28–37. [[CrossRef](#)]
80. Fleig, J. The grain boundary impedance of random microstructures: Numerical simulations and implications for the analysis of experimental data. *Solid State Ion.* **2002**, *150*, 181–193. [[CrossRef](#)]
81. Baumann, F.; Fleig, J.; Habermeier, H.; Maier, J. Impedance spectroscopic study on well-defined (La,Sr)(Co,Fe) $\text{O}_{3-\delta}$  model electrodes. *Solid State Ion.* **2006**, *177*, 1071–1081. [[CrossRef](#)]
82. Escudero, M.J.; Aguadero, A.; Alonso, J.A.; Daza, L. A Kinetic study of oxygen reduction reaction on  $\text{La}_2\text{NiO}_4$  cathodes by means of impedance spectroscopy. *J. Electroanal. Chem.* **2007**, *611*, 107–116. [[CrossRef](#)]
83. Antonova, E.P.; Khodimchuk, A.V.; Usov, G.R.; Tropin, E.S.; Farlenkov, A.S.; Khrustov, A.V.; Ananyev, M.V. EIS analysis of electrode kinetics for  $\text{La}_2\text{NiO}_{4+\delta}$  cathode in contact with  $\text{Ce}_{0.8}\text{Sm}_{0.2}\text{O}_{1.9}$  electrolyte: From DRT analysis to physical model of the electrochemical process. *J. Solid State Electrochem.* **2019**, *23*, 1279–1287. [[CrossRef](#)]
84. Adler, S.B.; Lane, J.A.; Steele, B.C.H. Electrode kinetics of porous mixed-conducting oxygen electrodes. *J. Electrochem. Soc.* **1996**, *143*, 3554–3564. [[CrossRef](#)]
85. Gilev, A.R.; Kiselev, E.A.; Cherepanov, V.A. Oxygen transport phenomena in (La,Sr) $_2$ (Ni,Fe) $\text{O}_4$  materials. *J. Mater. Chem. A* **2018**, *6*, 5304–5312. [[CrossRef](#)]
86. Li, Z.; Haugsrud, R.; Norby, T. Oxygen bulk diffusion and surface exchange in Sr-substituted  $\text{La}_2\text{NiO}_{4+\delta}$ . *Solid State Ion.* **2011**, *184*, 42–46. [[CrossRef](#)]